High precision ²⁶Al- 1²⁶Mg chronology of chondrules in unequilibrated 2 ordinary chondrites: evidence for restricted formation ages 3

Guillaume Siron^{a*}, Kohei Fukuda^a, Makoto Kimura^b, and Noriko T. Kita^a

5

4

6^a WiscSIMS, Department of Geoscience, University of Wisconsin-Madison, Madison, WI 53706, 7

USA

8 National Institute of Polar Research, Meteorite Research Center, Midoricho 10-3, Tachikawa, 9 Tokyo 190-8518, Japan

10

- 11 *corresponding author: guillaume.siron@unibo.it
- 12 *Current address: via Zamboni 67, 40126 Bologna

13

14 ABSTRACT

15

16 Chondrules in ordinary chondrites are considered to form in high density environments, 17 likely related to the evolution of protoplanets and large planetesimals. In order to determine the 18 timing of their formation at high time resolution (≤ 0.1 Ma), we conducted high precision Al-Mg 19 chronology of 17 porphyritic chondrules from 6 different unequilibrated ordinary chondrites 20 (UOCs) of low petrologic subtypes (3.00-3.05). Detailed petrology, mineralogy, and oxygen 21 isotope ratios of individual chondrules were also obtained that include 10 additional chondrules 22 without Al-Mg ages. Seventeen chondrules for Al-Mg chronology consist of 14 chondrules with 23 plagioclase (An₁-An₈₇) and three chondrules with Na-rich glassy mesostasis, all of which have high 27 Al/ 24 Mg ratios (30-3,000). The inferred initial (26 Al/ 27 24 Al)o ratios range between (6.5 ± 0.6)×10⁻⁶to (9.5 ± 1.0)×10⁻⁶, corresponding to chondrule formation ages of 1.74 ± $^{0.12}$ 25 /_{0.11} Ma to

 2.13 ± 0.09 Ma after CAIs, which have a canonical (26 Al/ 27 Al)0 ratio of 5.25×10^{-5} 26. Six albite 27 bearing chondrules (An<30) show a much more restricted ages range, spanning between $2.00 \pm$

 $^{0.11}$ / $_{0.10}$ Ma and $2.07 \pm ^{0.11}$ 28 / $_{0.10}$ Ma. Including 14 anorthite-bearing chondrules studied previously, 29 chondrules in ordinary chondrites have a restricted range of formation ages from 1.8 Ma to 2.2. 30 Ma after CAIs.

31 Based on the newly acquired oxygen isotope data and previous high precision studies, chondrules in L and LL chondrites do not show systematic difference in their δ^{18} O and δ^{17} 32 O 33 signatures. Majority of plagioclase-bearing chondrules studied for Al-Mg chronology show similar 34 oxygen isotope ratios to those of glass-bearing chondrules. There is no obvious difference in Al 35 Mg ages of chondrules between L and LL chondrites. Thus, chondrules in L and LL chondrites 36 would have formed in common environments and processes, though they accreted to two separate 37 parent bodies by 2.2 Ma after CAIs, which timing is consistent with the proposed thermal model 38 for ordinary chondrite parent bodies. Onset of chondrule formation at 1.8 Ma after CAIs may be 39 caused by the delay of Jupiter formation or the formation of protoplanets in ordinary chondrite 40 chondrule forming regions if chondrules formed by large scale disk shock or impact jetting of 41 protoplanets. Alternatively, early formed chondrules would not be preserved before 1.8 Ma if 42 chondrules formed by the impacts of molten planetesimals.

44 1. INTRODUCTION

45

43

46 Chondrules are one of the most ubiquitous components of chondrites. They are believed to 47 represent solidified melt droplets resulting from transient high temperature heating of dust 48 aggregates in the protoplanetary disk (Grossman, 1988; Jones, 2012; Connolly and Jones, 2016). 49 Several models have been proposed to explain the chondrule formation mechanism and this has 50 been a highly debated subject for decades (Krot et al., 2005; Morris et al., 2012; Desch et al., 2012; 51 Johnson et al., 2015). One of the key constraints to decipher the chondrule formation mechanism 52 is the time and duration of chondrule formation. Alexander et al. (2008) and Alexander and Ebel 53 (2012) showed that Na-rich chondrules in unequilibrated ordinary chondrites (UOCs) formed in a 54 dense environment, which would immediately (i.e. < 0.1 Ma) be accreted into parent asteroidal 55 bodies. Such short duration would prevent any large-scale mixing of material in the protoplanetary 56

disk (Cuzzi et al., 2010). A very useful chronometer to decipher the early evolution of the solar system is the 26 Al 26 Mg system due to its very short half-life (7.05×10⁵

57 y; Nishiizumi, 2004). Earlier ²⁶Al- 58 ²⁶Mg studies have shown UOC chondrule formation ages ranging between 1.2-3 Ma 59 after CAIs (Hutcheon and Hutchison, 1989; Hutcheon and Jones, 1995; Kita et al., 2000; Villeneuve et al., 2009; Kita and Ushikubo, 2012; Pape et al., 2019). The ²⁰⁶Pb ²⁰⁷ 60 Pb chronometers 61 of UOC chondrules indicate even longer duration of chondrule formation, 0-4 Ma after CAI 62 (Bollard et al., 2017).

63 Recently, Siron et al. (2021) studied UOC chondrules that contain relatively coarse (≥10 64 µm) anorthite in order to eliminate the potential disturbance to the Al-Mg system caused by parent 65 body metamorphism since Mg isotopic diffusion is much slower in anorthite than glass or Na-rich plagioclase (Van Orman et al. 2014). The ²⁶Al- 66 ²⁶Mg isotope measurements were optimized for 67 coarse anorthite analyses by using moderate beam sizes (6 µm and 15 µm) and combining Faraday 68 cup (FC) and electron multiplier (EM) detectors on multi-collection system. This allowed us to 69 obtain ages with uncertainties in the range of 0.04-0.15 Ma, two to five times better than most ages in previous studies. The 26 Al 26 Mg ages ranged between 1.80 \pm 0.04 Ma and 2.16 \pm $^{0.12}$ 70 /0.11 Ma 71 after CAIs, in agreement with the range reported by Kita et al. (2000) but much shorter than those 72 of Villeneuve et al. (2009) and Pape et al. (2019), although most chondrules were within 73 uncertainties of this range for the two studies. Within this short timescale, the very high precision 74 allowed them to highlight at least two chondrule forming events at ~1.9 and 2-2.15 Ma. While anorthite-bearing chondrules show a wide range of chondrule textures and mineral 76 compositions, they are uncommon chondrule types in UOCs with a depletion of volatile elements, 77 such as alkalis and Mn (Siron et al. 2021). Thus, chondrule formation events indicated from the

²⁶Al- 78 ²⁶Mg ages of anorthite-bearing chondrules would potentially not represent that of typical 79 chondrules in UOCs with higher abundance of alkali and volatile elements. A similar approach 80 and method on more representative chondrule compositions is required to constrain the true range 81 of UOC chondrule formation ages.

In this study, we present $^{26}\text{Al-}\ 82$ ^{26}Mg measurements of UOC chondrules that contain Na-rich 83

mesostasis, which are the most common type of chondrule in ordinary chondrites (Ikeda, 1983).

Porphyritic chondrules with mesostasis that contain plagioclase or glass with high ²⁷Al/ 84 ²⁴Mg ratios 85 (≥30) were selected among several L/LL3.00-3.05 UOCs. They are primarily plagioclase-bearing 86 chondrules, which makes up of about 20% of UOC chondrules (Lewis and Jones 2019), and also 87 include some glass-bearing chondrules that are similar to those previously studied.

88

89 **2. METHODS**

90

91 **2.1 Samples**

92

93 The UOCs selected for this study have all been classified as subtypes 3.00-3.05 from their 94 Cr₂O₃ contents in olivine (Grossman and Brearley, 2005). They include one fall, Semarkona 95 (LL3.00), three desert finds, Northwest Africa (NWA) 7731 (L3.00), NWA 8276 (L3.00) and 96 NWA 8649 (LL3.05), and three Antarctic finds, Queen Alexandra Range (QUE) 97008 (L3.05), 97 Meteorite Hills (MET) 00452 (L/LL 3.05), and MET 00526 (L/LL 3.05). The olivine Cr₂O₃ 98 content data for Semarkona, QUE 97008, and MET 00526 were reported in Grossman and 99 Brearley (2005). MET 00452 is a pair with MET 00526. The olivine Cr₂O₃ content data for NWA 100 7731 are reported in Agee et al. (2013), and those for NWA 8276 and NWA 8649 are in 101 Meteoritical Bulletin (Ruzicka et al., 2017). NWA 8276 is potentially a pair with NWA 7731. 102 Semarkona and QUE 97008 were classified as subtypes 3.01 and 3.05, respectively, based on Fe 103 Ni metal texture and chemistry which is a more sensitive method to estimate parent body thermal 104 metamorphism for types 3.00-3.15 chondrites (Kimura et al., 2008). In addition, we also examined 105 metal phases of Lewis Cliff (LEW) 86134 (L3.0) (Antarctic find). A summary of the meteorites, 106 sections and number of chondrules analyzed can be found in Table 1. These were the exact same 107 sections used in Siron et al. (2021).

108

109 **2.2 Electron microscopy**

111 To identify suitable locations for Al-Mg analyses, backscattered electron (BSE) and 112 secondary electron (SE) images were acquired using a Hitachi 3400 variable pressure scanning
113 electron microscope (SEM). More than 800 chondrules from multiple UOC sections were 114 examined using energy dispersive X-ray spectroscopy (EDS) spectra and BSE images in order to 115 find suitable chondrules for Al-Mg analyses that contain clean plagioclase or Al-rich glass that are

large enough to locate the 4 or 6 µm SIMS spots and have low Mg contents and thus high ²⁷Al/ 116 ²⁴Mg 117 (> 30 for FC-EM and >50 for MCEM). This allowed to restrict the number of chondrules to check 118 afterwards with the EPMA. Several EDS spectrums of olivine, pyroxene, plagioclase and glass 119 were obtained for each chondrule with counting times of 8 seconds. These EDS spectrums are 120 available in an open access repository listed in the Research Data section. 121 Major and minor element analyses were obtained for 89 selected chondrules at the Eugene 122 Cameron Electron Microprobe Laboratory of the University of Wisconsin-Madison using 15 kV 123 and 15 nA beam conditions. Eighteen chondrules had both their mesostasis and mafic minerals 124 measured, 20 glass-bearing chondrules had only their glass composition measured and 41 125 chondrules had only their mafic minerals measured. These chondrules were measured during the 126 same sessions to those reported in Siron et al. (2021). Plagioclase analyses were obtained during 127 three different sessions. The first and third sessions used the Cameca SX5 Field Emission gun 128 microprobe used a beam size of 3 µm, the second session using the Cameca SX51 microprobe with 129 a beam size of 5 µm, both are equipped with 5 wavelength dispersive spectrometers. Counting 130 times were 10 seconds on the wavelength peak and 5 seconds on both backgrounds (before and 131 after peak), except for Al and Ti measurements in the second session that were measured using the 132 mean atomic number (MAN) method (Donovan et al., 2016), for which no background is required. 133 During this second session, counting times were reduced for Na, K and Mn to 5 seconds on both 134 backgrounds and peak and increased to 20 (peak) and 10 (backgrounds) seconds for Mg. The full 135 list of standards was described in Siron et al. (2021). Glass analyses were performed during the 136 third session on the SX5 with a cryogenic stage in order to avoid any Na2O loss during glass 137 analyses.

138 The data were reduced using the Probe software package using ZAF and $\varphi \rho z$ matrix 139 correction routines together. In this paper, all uncertainties for major and minor elements are given 140 in 1 standard deviation (1SD) and represent averages of multiple analyses. Plagioclase end 141 members, including excess silica (Beaty and Albee, 1980; Tenner et al., 2019) were computed 142 using the algebraic method described in Siron et al. (2021). In this paper, An was computed as Ca 143 / (Ca + Na +K) × 100 for plagioclase.

144 For the evaluation of subtype through Fe-Ni metal in individual chondrites presented in 145 this paper, BSE images were acquired using a JEOL JSM-5900 LV scanning electron microscope 146 at the National Institute of Polar Research. The number density and average area of Ni-rich metal 147 grains inside chondrules were determined from one section of LEW 86134, QUE 97008, NWA 148 8276 and 7731, MET 00452 and 00526 and two polished mounts of NWA 8649. The number 149 density represents the number of Ni-rich metal grains per unit area for individual metal spherules (N/μm² 150). The average area is computed from the different individual Ni-rich areas inside each 151 metal spherule. An average from several metal spherules was computed for every mount or section. 152 Small (<10 μm) plagioclase and glass in chondrules that were selected for SIMS analyses 153 had their locations marked by a focused ion beam (FIB) technique. We used a field emission gun 154 SEM Zeiss Auriga with FIB capability at the Nanoscale Imaging and Analysis Center, University 155 of Wisconsin-Madison by following the procedures described in Hertwig et al. (2019). A 3 × 3 μm² 156 square platinum deposition was first applied to the location of plagioclase or glass, guided by SEM images of chondrules. Then, a 1 × 1 μm²

157 square area at the center of the platinum deposition along with the underlaying carbon coating (20 nm thickness) was removed by a focused Ga⁺ 158 ion

beam at 30 keV and 5 pA with a duration of 90 seconds (dose of 0.4 nC/ μ m² 159). These FIB marks were later located by SIMS ²⁷Al⁺

160 ion imaging for accurate targeting of SIMS primary beam 161 positions for Al-Mg isotope analyses.

162

163 **2.3 SIMS Oxygen isotopes**

165 Oxygen three-isotope measurements were conducted using the IMS1280 at the WiscSIMS 166 laboratory of the University of Wisconsin-Madison during two separate sessions under similar 167 analytical conditions. Part of the data collected in the second session were for anorthite-bearing chondrules that were already reported in Siron et al. (2021). A ~2 nA focused gaussian Cs⁺ 168 primary beam was used, resulting in secondary intensity of (2-3)×10⁹ counts per seconds (cps) for ¹⁶O⁻ 169 . 170 The beam spot size was about $12 \times 10 \,\mu m$ in diameter for both sessions. A mass resolving power (MRP) of ~5000 was achieved in order to sufficiently resolve ¹⁷O peak from ¹⁶O¹ 171 H interference. 172 All three oxygen isotopes were detected simultaneously by using multi-collector Faraday cups (MCFC) with feedback resistors of 10^{10} and 10^{11} Ω for 16 O and 18 O, respectively, and 10^{12} 173 Ω for 17 O in order to reduce thermal noise (e.g., Fukuda et al., 2021a). Additionally, the ¹⁶O¹ 174 H signal was measured at the end of each analysis to estimate its tailing effect on ¹⁷ 175 O signals. As for 176 previous studies, 12-18 unknown chondrule measurements were bracketed by 8 analyses of San 177 Carlos olivine (SC-Ol) standard (Hertwig et al., 2018). No drift correction was required during the 178 first session, while a small correction was made for the second session based on repeated analyses 179 of SC-Ol running standard. The detail description of the correction was reported in Siron et al. 180 (2021) and corrected data are shown in EA1 Table S1-3. The reproducibility of SC-Ol standard

measurements in both sessions was typically 0.2% for δ^{18} O and 0.25% for δ^{17} O and Δ^{17} 181 O (after 182 drift correction for the second session).

183 Five additional olivine standards (from Fo₀ to Fo₁₀), 4 low-Ca pyroxenes (from En₁₀ to 184 En₂₁) and one diopside standard (Kita et al., 2010; Fukuda et al., 2020) were analyzed at the 185 beginning of the session to correct matrix effect related to the mineral compositions. In the first 186 session, the instrumental biases of olivine and low-Ca pyroxene show a small positive correlation 187 with Fo or En compositions, respectively (EA1 Table S1), similar to those observed in the past 188 study (e.g., Tenner et al., 2015). In the second analysis session, the instrumental biases among 189 olivine standards were nearly the same (≤±0.3‰) within the range of compositions (EA1 Table 190 S2), so that no additional bias correction depending on Fo contents was applied. Similarly, no 191 significant matrix effect was found for low-Ca pyroxenes standards for such a limited range of En 192 compositions. Correction of

matrix effect for Ca content was achieved using the one diopside 193 standard.

194 Uncertainties for each individual analysis were estimated by propagating the 2SD of the 195 standard measurements bracketing the analysis, the 2SE of these standard analyses, the uncertainty 196 on the fit (95% confidence interval) when corrected for drift and an additional factor of 0.3% to 197 account for the error on the reference values for standards from laser fluorination. Host chondrule 198 oxygen isotopic compositions were computed (EA1 Table S4) following the procedure established in Ushikubo et al. (2012) and Tenner et al. (2013). During both sessions, the 3SD for Δ^{17} 199 O of the SC-Ol of all measurements was 0.43%. A first mean Δ^{17} 200 O value taking all analyses for a chondrule 201 was computed and used to identify analyses that are outside of 3SD (0.43%) from the mean. Data 202 are rejected if the rest of analyses are all within 3SD limit of their mean value. The remaining analyses are used to compute mean oxygen isotope ratios (for δ^{18} O, δ^{17} O, and Δ^{17} 203 O), which are 204 assigned as those of host chondrules oxygen isotope ratios. As for individual analyses, the 205 uncertainty on the host chondrule composition for each chondrule is the propagation of 2SE of n 206 individual measurements inside one chondrule and the additional uncertainties of instrumental mass fractionation; 0.3% and 0.15%, for δ^{18} O and δ^{17} 207 O, respectively (Kita et al., 2010).

208

209

210 **2.4 SIMS Al-Mg isotopes**

211

212 All Al-Mg isotope measurements were conducted using the IMS 1280 at the WiscSIMS 213 Laboratory of the University of Wisconsin-Madison. Conditions for analyses are similar to those 214 in previous studies (Kita et al., 2012; Hertwig et al., 2019; Fukuda et al., 2020) and some of the

analyses were conducted during the same sessions as data reported in Siron et al. (2021) . The O_{2} - 215

216 primary ions were focused in Gaussian mode with a 23 kV impact energy (-13 kV at the ion source 217 and +10 kV at the sample surface) from the RF plasma ion source. Transfer optics were tuned 218 using a Max Area of 40 μ m (magnification × 200). Entrance slits were set to 90 μ m and exit slits 219 to

500 μ m, which provides a MRP of ~2200 (M/ Δ M). Although this MRP setting is lower than 220 that required for Mg hydride interferences, Hertwig et al. (2019) confirmed that interference from hydride and 48 Ca²⁺ are sufficiently small compared to Mg⁺ 221 signals.

Delta notation δ²⁵Mg and δ 222 ²⁶Mg used absolute Mg isotope ratios to normalize raw data as follow (²⁵Mg/²⁴Mg) = 0.12663 and (²⁶Mg/ 223 ²⁴Mg) = 0.13932 (Catanzaro et al., 1966). Instrumental 224 bias was corrected using several standards matching the matrix of measured olivine, pyroxene, glass and plagioclase. The excess ²⁶Mg after mass fractionation correction (δ²⁶Mg* 225) was calculated 226 using an exponential law in two steps, similarly as Hertwig et al. (2019) and as follow: 227

$$\mathbf{229} (2) 230$$

231 The exponential parameter β was assumed to be 0.5128 (Davis et al., 2015) for plagioclase 232 analyses and determined from olivine standards for olivine and pyroxene analyses, see Supplementary Material in Siron et al. (2021). The $\delta^{26} Mg^*$ is equivalent to Δ 233 $^{26} Mg$ when the natural mass dependent fractionation measured as δ 234 $^{25} Mg$ equals zero (Ushikubo et al., 2017). Following 235 the procedure of Tenner et al. (2019), we assume chondrules do not have a significant natural mass dependent fractionation in $\delta^{25} Mg$ and estimated $\delta^{26} Mg^*$ from Δ 236 $^{26} Mg$.

237 The relative sensitivity factors (RSFs) of standards were used to correct for instrumental 238 bias as follow:

239

242 Three different analytical settings were used, two for plagioclase and glass measurements 243 with 4 μ m and 6 μ m spot sizes, respectively, and one for olivine and pyroxenes with 8 μ m spot size. In all sessions, three Mg isotopes and 27 Al⁺

244 signals were detected simultaneously on the 245 multicollection (MC) system. Mg isotope signals were detected by using three electron multipliers (EMs) for 4 μ m spot size (MCEM), one FC for ²⁴Mg and two EMs for ²⁵Mg and 246 ²⁶Mg for 6 μ m

spot size (FC-EM), and three FCs for olivine and pyroxene analyses (MCFC). The ²⁷Al⁺ 247 signal 248 was always detected by FC.

249

250 2.4.1. MC FC-EM analyses of mesostasis (6 µm spot size)

251 This analytical setting was optimized for plagioclase and glass that are ~10 μ m in size with MgO contents of 0.4-1.0 wt.% and 27 Al/ 252 24 Mg of 30-100. Two sessions were conducted using a 253 spot size of ~6 μ m with a primary intensity of ~160 pA at the same time when the majority of the data reported in Siron et al. (2021) were collected. The secondary 24 Mg⁺and 27 Al⁺ 254 intensities were typically (6-8)×10⁵cps and ~2×10⁷

255 cps for a synthetic anorthite glass standard with 1.0 wt.% MgO (AnG+1.0%; Kita et al., 2012). FC detectors with $10^{12} \Omega$ and $10^{11} 256 \Omega$ resistances were used for 24 Mg⁺and 27 Al⁺, respectively. EMs were used for measurements of 25 Mg⁺and 26 Mg⁺257 isotopes, with secondary ion intensities of 7×10^4 cps to 1×10^5

258 cps for 1.0 wt.% MgO standard. Analyses 259 typically consisted of 120 s of presputtering followed by centering of secondary ion deflectors and

400 cycles of 4s of counting times. During presputtering, the FC baseline was measured for $^{24} \rm Mg^+260$

and an average of 8 analyses was used to correct ²⁴Mg⁺ 261 intensities. The background variations 262 were typically ~150-180 cps (1SD). The overall analysis

time was ~32 min. In order to maintain constant EM gains relative to FC detectors, high voltage (HV) of each EM was adjusted at the 20th 263 and 220th 264 cycles using a Cameca software routine. The gain drift for each EM was monitored and 265 corrected using a second discriminator connected parallel to the first one (see detail information 266 in SM2-1).

267 Two synthetic anorthite composition glass standards with 0.6 and 1.0 wt.% MgO contents 268 (AnG+0.6% and AnG+1.0%) were used to correct for instrumental bias on Mg isotopes and ²⁷Al/ 269

 ^{24}Mg RSF (Kita et al., 2012). These standards have MgO content similar to the unknown plagioclase and glass in chondrules and no matrix effect for Δ 270 ^{26}Mg was found between anorthite glass and labradorite mineral standards. Internal errors were typically 0.4-0.6% (2SE) for Δ 271 ^{26}Mg and 0.5-1 % for $^{27}\text{Al}/$ 272 ^{24}Mg ratios. As described in Siron et al. (2021), the measured Mg isotope

273 ratios of standards drifted over time during each of the two analytical sessions. This drift was 274 corrected using a weighted least square algorithm (results are shown in EA1 Table S5; see Siron 275 et al., 2021 for more explanations). The second day of analysis did not require any drift correction, 276 as well as the second session. Reproducibility for standard analyses were typically 0.4-0.7% (2SD)

for Δ 277 ²⁶Mg (after drift correction whenever the corrections were applied). Two analyses of 278 chondrule glass in this study touched a high-Ca pyroxene and were stopped before the end of the 400 cycles. For these analyses, only the cycles before abrupt increase of Mg⁺ 279 were taken to calculate Δ^{26} Mg and ²⁷Al/²⁴Mg ratios and the standard analyses used for calibrating δ^{26} Mg^{*} 280 were also recalculated using the same number of cycles since ²⁷Al/²⁴Mg and Δ 281 ²⁶Mg values changed with the

depth of analysis (Hertwig et al., 2019). Final uncertainties for δ^{26} Mg* 282 represent the 283 propagation of internal error (2SE), error on the fit for drift correction at the time of the analysis if 284 a drift correction was necessary (95% confidence interval) and 2SE of the standard measurements 285 for the day of analysis. This final uncertainty is largely dominated by the internal error. Since no

drift correction was applied for ²⁷Al/ 286 ²⁴Mg ratios, its uncertainty represents the propagation of 287 internal error (2SE) and 2SE of the standard measurements for the day. Again, this uncertainty is 288 dominated by the internal error.

290 2.4.2. MCEM analyses of mesostasis (4 µm spot size)

291 This analytical setting was optimized for plagioclase and glass that are smaller than 10 μ m in size with MgO contents from ~0.01 wt.% to ~1 wt.% and 27 Al/ 292 24 Mg \geq 30, similar to those in Hertwig et al. (2019). An O_2 -primary intensity of 45 pA resulted in secondary 24 Mg⁺and 27 Al⁺ 293

intensities of $\sim 2 \times 10^4$ cps and $\sim 6 \times 10^6$ 294 cps for a natural labradorite (Ans9) standard Lab1 (~ 0.1 wt.% MgO; Kita et al., 2012) and 24 Mg⁺intensity was as high as 1.7×10^5

295 cps for AnG+1.0% standard. 296 Three EM detectors (L2, L1, and C) were used for all three Mg isotope signals and a FC detector (H2p) was for ²⁷Al⁺ with a 10¹¹ 297 Ω resistance. The analyses consisted of 100 sec of presputtering, 298 followed by the alignment of secondary ion deflectors and 240 cycles of 10 seconds of counting 299 each. The overall analysis time was ~45 min. In order to maintain constant EM gains during the entire session, high voltage (HV) of each EM was adjusted at the 20th 300 cycle using the Cameca 301 software routine. The gain drift for each EM was monitored and corrected using a second 302 discriminator connected parallel to the first one (see detailed information in SM2-1). Three 303 standards with a range of MgO contents covering the range of samples were used to correct for 304 instrumental bias, Lab1 with lowest MgO (~0.1%), AnG+0.6%, and AnG+1.0%. A single analysis 305 session was conducted in the sequence that (1) chondrule plagioclase with lowest MgO («0.1%) 306 bracketed by Lab1 as running standard, (2) chondrule plagioclase and glass with intermediate MgO 307 (0.1-0.3%) bracketed by Lab1 and AnG+0.6%, and (3) chondrule glass with higher MgO (0.6-1%)

bracketed by AnG+0.6% and AnG+1.0%. Internal errors for Δ 308 ²⁶Mg were a strong function of MgO 309 content, they ranged from ~0.6% for AnG+1.0% to ~1.6-2% for Lab1 standard (~0.1% MgO). The reproducibility of ²⁷Al/ 310 ²⁴Mg ratios of three glass standards were typically within 1% (2SD) 311 and the RSF calculated from each standard agrees with each other within 1% (EA1 Table S6). As 312 for FC-EM analyses, the analysis was stopped when a measurement touched a high-Ca pyroxene grain and only the same number of cycles for the standards were used to correct for Δ 313 ²⁶Mg and ²⁷Al/ 314

²⁴Mg ratios. Of the 9 days of analyses, only two days required a slight drift correction 315 following the same procedure as for FC-EM data. The error was propagated similarly as for FC 316 EM data.

317

318 2.4.3. MCFC analyses of olivine and pyroxenes (8 µm spot size)

319 The Mg isotope analyses of olivine and pyroxene in this study were conducted together 320 with the chondrule analyses reported in Siron et al. (2021), in which details of the analytical setting were described. An O_{2^-}

321 with a primary intensity of 1nA and beam size of \sim 8 µm was used, which resulted in a secondary $^{24}\text{Mg}^+\text{intensity of} \sim 2\times 10^8$

322 cps for olivine and low-Ca pyroxene. We used

multicollector FC detectors with a $10^{10}\,\Omega$ resistor for $^{24}Mg^+$ and $10^{11}\,\Omega$ resistors for $^{25}Mg^+$, $^{26}Mg^+$ 323

and ²⁷Al⁺

324 . The analyses consisted of 100 sec of presputtering, followed by the alignment of 325 secondary ion deflectors and 30 cycles of 10 seconds. The overall analysis time was \sim 8 min. 326 Fifteen different olivine standards (Fo60-Fo100) and 5 pyroxene standards (two diopside and three 327 low-Ca pyroxenes; En85-En97) were used to correct for natural and instrumental bias (Fukuda et 328 al., 2020). The power for the mass dependent fractionation law β was determined using terrestrial

olivine standards to be 0.5169. Small drift of the Δ 329 26 Mg values during the session was evaluated 330 using SC-Ol running standard under the same procedure as for FC-EM and MCEM analyses. We applied a correction due to a small offset on raw Δ 331 26 Mg* among terrestrial olivine and pyroxene 332 standards with values $0.019 \pm 0.010\%$ (2SE) and $0.150 \pm 0.025\%$ (2SE), respectively, relative to 333 the SC-Ol standard (Siron et al., 2021). These instrumental bias corrections are described in detail in Siron et al. (2021). Internal errors for Δ 334 26 Mg were typically 0.04-0.07‰ and 0.06-0.15‰, for 335 olivine and pyroxene analyses, respectively. Reproducibility of standard measurements was 336 typically 0.04-0.06‰ (2SD) for SC-Ol standard, after drift correction. The error propagation was 337 the same as those used for plagioclase and glass measurements.

339 2.4.4 Isochron regression

340 Isochron regressions were computed using the online version of IsoplotR (Vermeesch, 341 2018) with the maximum likelihood option, i.e. Model 1 (York et al., 2004). Uncertainties on ²⁷Al/ 342 ²⁴Mg used for the regression did not take into account the uncertainty on the reference value 343 (from EPMA measurements) on RSF for plagioclase glass and mineral standards since this 344 uncertainty is a systematic uncertainty. This would have prevented any conclusion based on 345 MSWD (mean square weighted deviation) for the goodness of fit. To account for this systematic 346 uncertainty from RSF, a 6% error from EPMA analyses of Lab1 (Ana) standard (Kita et al. 2012) 347 was added to the uncertainty on the slope for plagioclase-bearing chondrule with An content higher 348 than An 30. The RSF among AnG+1.0%, AnG+0.6%, and Lab1 standards analyzed in this work 349 were indistinguishable (EA1 Table S5) and it is known that RSF among most silicate mineral and 350 glass standards agree within 10% (e.g., Kita et al., 2012; Pape et al., 2019; Fukuda et al., 2021b). 351 Therefore, the same RSF from Lab1 standard was applied to more albitic plagioclase as well as 352 for Na-rich glass-bearing chondrules. However, applied RSF values were extrapolated beyond the 353 compositional range of standards, so that we applied a larger uncertainty of 10% to the final 354 isochron slopes as in the previous study (Hertwig et al., 2019).

355

356

357 **3. RESULTS**

358

360 ²⁶Mg dating in this study. They were selected among 63 chondrules that contain crystalline plagioclase and/or glass with high ²⁷Al/ 361 ²⁴Mg ratios. The selection criteria were the 362 presence of multiple regions (n≥5) of clean plagioclase or high Al/Mg glass larger than > 5 µm. 363 This was meant to analyze individual glass or plagioclase in chondrules without overlapping with 364 mafic minerals, which are critical in obtaining reliable Al-Mg isochron regression lines. Among 365 them, seven chondrules are from QUE 97008, four from NWA 8649, three from NWA 8276, and 366

359 Seventeen chondrules, from 6 different chondrites, were investigated for oxygen isotopes and ²⁶Al-

one each from NWA 7731, MET 00452, and Semarkona. Of these chondrules, 14 have plagioclase 367 as the main mesostasis phase and 3 have glass dominating mesostasis. Of the 14 plagioclase 368 bearing chondrules, 3 had residual melt that could be analyzed for major and minor elements and 369 Al-Mg isotopes. Both glass and plagioclase areas were always too small to be analyzed with the 370 12 µm spot size required for high precision oxygen three-isotopes. In addition to these 17 371 chondrules, 10 chondrules from NWA 7731 were analyzed for oxygen isotopes.

372

373 3.1 Petrographic description

374

375 Figures 1-3 show the selected chondrules studied for Al-Mg and oxygen isotopes that 376 contain either plagioclase or small areas of glassy mesostasis. They are mostly similar to 377 plagioclase-bearing chondrules described in Lewis and Jones (2019) but are very different from 378 Na-Al-rich chondrules described in Bischoff and Keil (1984) and Ebert and Bischoff (2016) that 379 have large areas of Na- and Al-rich mesostasis. Tables 2-5 represent the olivine, pyroxene, 380 plagioclase and glass compositions, respectively. Olivine and low-Ca pyroxene in these chondrules 381 show Mg# (defined as molar [Mg]/[Mg+Fe] %) between 75 and 96 and between 81 and 97, 382 respectively. Of the 17 chondrules selected for Al-Mg analyses, 5 are FeO-poor (type I; Mg#≥90) 383 and all others are FeO-rich (type II; Mg#<90). All five type I chondrules, i.e., NWA 8649 c62 384 (Fig. 1a), QUE 97008 c12 (Fig. 1b), c41 (Fig. 1c) and c68 (Fig. 1d), and NWA 8649 c27 (Fig. 1e) 385 are porphyritic pyroxene (PP, i.e., less than 20% of olivine). On the other hand, only a few type II 386 chondrules are PP chondrules, i.e., QUE 97008 c134 (Fig. 1f) and NWA 8649 c12 (Fig. 1g). They 387 have similar textures to their type I counterparts. The vast majority of type II chondrules are 388 porphyritic olivine pyroxene (POP, i.e., between 20-80% of olivine), i.e., NWA 7731 c33 (Fig. 389 1h), NWA 8276 c22 (Fig. 2a) and c43 (Fig. 2b), QUE 97008 c102 (Fig. 2c) and c140 (Fig. 2d), 390 and Semarkona c55 (Fig. 2e). There is only one porphyritic olivine chondrule (PO, i.e., more than 391 80% of olivine), MET 00452 c85 (Fig. 2f). Pyroxene and olivine proportions were qualitatively 392 estimated from BSE images. Type II chondrules show higher internal variations in Mg# than type 393 I due to a strong zoning of olivine toward the edge. In most cases, Mg# of olivine and low-Ca 394 pyroxene are in good agreement in each chondrule, even for zoned olivine, where core Mg# of 395 olivine and low-Ca pyroxene are very similar. All 3 glass-bearing chondrules are type II 396 chondrules, QUE 97008 c31 (Fig. 2g) and NWA 8649 c116 (Fig. 2h) are type II PP chondrules 397 while NWA 8276 c59 (Fig. 3a) is a type II POP chondrule. A few chondrules have plagioclase 398 grains that are zoned. NWA 8649 c27 has one large grain (15-20 μm thick) that exhibit a core and 399 rim with two different plagioclase compositions, i.e., An₇₀ for the core and An₅₈ for the rim, and a 400 sharp boundary between the two. All smaller grains are homogeneous in An contents and only 401 exhibit the rim composition of the larger grain. QUE 97008 c41 also exhibits a minor 402 compositional zoning in plagioclase as seen by the larger 1SD of the An content among the 7 403 EPMA analyses, though it is difficult to definite composition for each zone due to the narrow 404 thickness of only 5-10 μm.

405 We note that many plagioclase-bearing chondrules show textures for their mafic minerals 406 that are very similar to glass-bearing chondrule textures. For example, type II PO chondrule MET 407 00452 c85 (Fig. 2f) shows a porphyritic texture very similar to those of typical glass-bearing type 408 II PO chondrules. Large olivine grains show sharp, straight, mineral faces, with some corrosion 409 gulf. Additionally, the presence of small pyroxene grains (Fig. 3b) around large olivine 410 phenocrysts is not uncommon for type II PO glass-bearing chondrules, as can be seen for MET 411 00526 c65 (Fig. 3c). Another example, plagioclase-bearing type II POP chondrule Semarkona c55 412 (Fig. 3d) shows petrolographical textures very similar to another type II POP glass-bearing 413 chondrules NWA 7731 c52 (Fig. 3e). The presence of olivine chadacrysts in low-Ca pyroxene, the 414 elongated and rounded olivine grains, and their zoning toward the edge (Figs. 3d-e), are all 415 strikingly similar between these two chondrules that differ only by their mesostasis mineralogy; 416 plagioclase in Semarkona c55 (Fig. 3d) and glass in NWA 7731 c52 (Fig. 3e).

417 Since most of the chondrules analyzed in this study are Antarctic and Northwest African 418 finds (except for one chondrule in Semarkona), they almost all exhibit various degrees of terrestrial 419 weathering. It usually consists of fractures originating from the rim of the chondrules and filled 420 with a Fe-rich phase, clearly visible for chondrules NWA 8649 c62 (Fig. 1a) and c27 (Fig. 1e), 421 which are the most affected chondrules. Almost all chondrules have at least small fractures as for 422 NWA 8276 c43, highlighted with black arrows on Fig. 3f. Alteration of metal to magnetites are 423 seen among

several chondrules (e.g., NWA 8649 c27 and c116, QUE 97008 c31, c68 and c140), 424 either due to terrestrial weathering or aqueous alteration in parent body. Mesostasis of studied 425 chondrules do not show obvious alteration phases, such as phyllosilicates or nepheline replacement 426 of plagioclase (Lewis et al., 2022).

427 All individual analyses for major and minor elements from EPMA can be found in the 428 Supplementary Material (SM1 Table S9-12). The detailed petrographic description of the 429 chondrules analyzed for oxygen and Al-Mg isotopes can be found in the Supplementary Material 430 (SM2-2).

431

432

433 **3.2** Mesostasis composition

434

435 Figure 4 shows the composition of plagioclase from 51 chondrules, which include the 14 436 chondrules selected for Al-Mg analyses in this study. It also includes the composition of 19 437 anorthite-bearing chondrules that contain pure anorthite or close to pure anorthite (An>93), of which 438 14 are already reported in detail in Siron et al. (2021). The Mg# of olivine or pyroxene for the x 439 axis of Fig. 4a comes from EDS spectra and are slightly less accurate than EPMA data presented 440 in section 3.1. Additionally, they represent average compositions which does not take into account 441 zoning of type II olivine phenocrysts. One striking observation is the absence of albitic plagioclase 442 for high Mg# type I chondrules (Fig. 4a). Interestingly, no pure anorthite (i.e., above An95) can be 443 found for type I chondrules with high Mg# (≥95). There is a general tendency of increasing An 444 contents of plagioclase with chondrule Mg# among chondrules selected for the Al-Mg analyses in 445 this study; from low An ≤10 for chondrules with Mg#≤82 to the high An ~87 for NWA 8649 c62 446 with Mg# of 97. This contrasts with the consistently high An (≥93) for anorthite-bearing 447 chondrules studied by Siron et al. (2021) with a range of Mg# from 74 to 96. A similar tendency 448 between plagioclase An contents and chondrule Mg# has been observed among chondrules in 449 carbonaceous chondrites (Kurahashi et al., 2008; Ushikubo et al., 2013; Hertwig et al., 2019). The 450 chondrule from the common trend, i.e., increasing An content with increasing Mg#, shows a 451 general increase of MgO with increasing An content of plagioclase, from a very low MgO content
452 for pure albitic composition (0.01-0.2 wt.%) to a maximum value of 1.6 wt.% for An~95 (Fig. 4b).
453 However, in detail, there is a minimum close to the detection limit (~0.01 wt.%) at An10- An20. All
454 plagioclase-bearing chondrules selected in this study are on this trend. The second group of 455
chondrules consist mainly of anorthite-bearing chondrules studied by Siron et al. (2021) that all 456
show a restricted range of MgO between 0.5 and 1.0 wt.%. Very interestingly, there is no clear 457
tendency for the substitution responsible for (Fe,Mg) to enter the crystal structure of plagioclase
458 among those selected for Al-Mg in this study (Table 4). Both Ca(Mg,Fe)Si3O8 and 459
(Mg,Fe)Al2Si2O8 have very similar proportions, except for the highest An content plagioclase 460
bearing chondrule, NWA 8649 c62. This is in contradiction with what was observed for pure 461
anorthite-bearing chondrules where the end-member Ca(Mg,Fe)Si3O8 is heavily preferred (Siron 462 et al., 2021).

463 In Fig. 4c, excess silica ([]Si4O8) shows an inverted bell shape curve when plotted against 464 An content. The minimum for excess silica seems to be around An20-40. Again, the two trends 465 already described do not have the same evolution here. Indeed, excess silica decreases sharply with 466 An content for pure anorthite (Fig. 4c) while the decrease for the common trend is much less 467 pronounced. There seems to be an increase for pure albite composition toward maximum values 468 of 3% of []Si4O8, which correlates with the slight increase of MgO contents for pure albite 469 compared to those in An20-40. All chondrules studied for Al-Mg isotopes have low excess silica 470 (i.e., below 1%), except NWA 7731 with 1.8%. Some do not have any excess silica, such as QUE 471 98007 c12, c134 and core plagioclase composition of NWA 8649 c27 and plagioclase grains of 472 NWA 8649 c62. This is due to selecting a large number of chondrules having composition between 473 An30 and An60, where most plagioclases do not have excess silica.

474 Twenty-six glass-bearing chondrules investigated using EPMA in this study all have very 475 low MgO content (EA1-Table S12) and are all type II chondrules since the potential chondrules were narrowed after SEM investigation to low MgO content glass compositions to achieve ²⁶ 476 Al

²⁶Mg analyses with resolvable 477 ²⁶Mg excesses. Only three of them had Al/Mg ratios higher than 50 478 and were analyzed for their Al-Mg and oxygen isotopes using SIMS. This low number was

due to 479 the combination of setting a high Al/Mg threshold of 50 for EM-EM measurements and the fact 480 that many chondrules have mesostasis with small high-Ca pyroxene crystals which makes it hard 481 to find 5 μm areas without any crystals. One feature not commonly noted in literature is a 482 significant difference in K₂O contents between plagioclase and glass in chondrules. The 51 483 plagioclase-bearing chondrules analyzed in this study and Siron et al. (2021) show that the 484 orthoclase end-member is typically less than 1% (EA1 Table S11), with K₂O content mostly below 485 ~0.2 wt.%, and usually close or below the detection limit (~0.01 wt.%). On the opposite, K₂O glass 486 composition is fairly constant between 0.8 and 1.4 wt.%, without a strong correlation with Mg# of 487 olivine or pyroxene (Fig. 4d). Glass and plagioclase can be very easily distinguished by their 488 respective K₂O contents, in addition to the fact that glass analyses do not have a plagioclase 489 stoichiometry.

3.3 Fe-Ni metal

494 Results for the Fe-Ni metal characterization of the different chondrites studied here are 495 presented in the Supplementary Material (SM2-3). They all seem to be slightly more 496 metamorphosed than Semarkona (3.01; Kimura et al., 2008), even for those that were characterized 497 as 3.00 such as NWA 8276 and NWA 7731. When two sections were studied (NWA 8649 and 498 MET 00526), their results are in very good agreement (SM2-3). Additionally, QUE 97008 was 499 previously analyzed by Kimura et al. (2008) and the result from this study is also in very good 500 agreement with the previously published value. The data from this study cannot distinguish 501 between 3.05 and 3.10, thus the studied chondrites are grouped as 3.05-3.10. Nevertheless, some 502 of the chondrites are outside their respective errors and the least metamorphosed QUE 97008 503 seems to be slightly more pristine than NWA 8276 for example.

Table 6 shows the host chondrule values for δ^{18} O, δ^{17} O and Δ^{17} 508 O for all 17 chondrules 509 studied for Al-Mg isotopes as well as the 10 additional chondrules from NWA 7731 analyzed for 510 oxygen isotopes only. Figs. 5-7 show individual data for every chondrule analyzed for their oxygen 511 isotopes. BSE images of the spots after SIMS analyses as well as their location within the 512 chondrules can be found in Supplementary Material 3 (SM3).

513 Some chondrules are very homogeneous in oxygen isotope ratios and individual data points 514 cannot be distinguished from each other, resulting in host chondrule uncertainties similar to the 515 2SD of SC-Ol analyses bracketing the chondrule analyses (see EA1 Table S4). These chondrules 516 are QUE 97008 c41 (Fig. 5a), NWA 7731 c31 (Fig. 5b), c34 (Fig. 5c), c73 (Fig. 5d) and NWA 517 8649 c12 (Fig. 5e). Most other chondrules exhibit some internal variations outside their individual uncertainties for $\delta^{18} O$ and $\delta^{17} \, 518 \, O$. Some chondrules show variations without any clear trend such as $\, \, 519 \, \, NWA \, \, 8276 \,$ c43 (Fig. 5f), c59 (Fig. 5g), Semarkona c55 (Fig. 5h), MET 00452 c85 (Fig. 5i), NWA 520 8649 c27 (Fig. 6a), c116 (Fig. 6b), NWA 7731 c14 (Fig. 6c), c49 (Fig. 6d) and c52 (Fig. 6e). Some 521 exhibit variations following a mass dependent fractionation line with a slope of about 0.52 such as 522 QUE 97008 c102 (Fig. 6f), NWA 7731 c33 (Fig. 6g), NWA 8276 c22 (Fig. 6h), NWA 8649 c62 523 (Fig. 6i). Others show variations along a slope 1 line, such as QUE 97008 c31 (Fig. 7a), c140 (Fig. 524 7b), NWA 7731 c5 (Fig. 7c), c17 (Fig. 7d), c24 (Fig. 7e), c28 (Fig. 7f). Additionally, among the 525 type I or II PP chondrules in which olivine chadacrysts were analyzed, some of these chadacrysts had δ^{18} O and δ^{17} 526 O significantly deviated from the rest of the analyses, as it can be clearly seen for QUE 97008 c12 (Fig. 7g), c68 (Fig. 7h), c134 (Fig. 7i). These chadacrysts have a different Δ^{17} 527 O 528 than the low-Ca pyroxene and were always excluded from the host chondrule value. In two chondrules, QUE 97008 c12 and c134, one chadacryst has δ^{18} O and δ^{17} 529 O signatures similar to the low-Ca pyroxene analyses while another is different. In c134, the chadacryst has different δ^{18} 530 O and δ^{17} O values, while in c12 only δ^{18} 531 O is different from the host chondrule value.

532 The host chondrule oxygen isotope ratios of 27 chondrules are shown in Fig. 8 in oxygen

three-isotope diagrams. Type I chondrules show a wider range of variabilities in $\delta^{18}O$ and δ^{17} 533 O 534 compared to those of type II chondrules (Fig. 8a-b) in agreement with data previously reported for 535 LL3 chondrite chondrules by Kita et al. (2010). Most chondrules, including all type II chondrules, 536 plot on or slightly above the terrestrial fractionation line (TFL), between the Equilibrated 537 Chondrite Line (ECL, Clayton et al., 1991) and the Primitive Chondrule Minerals (PCM, Ushikubo et al., 2012) line with ranges of $\delta^{18}O$ and δ^{17} 538 O from 3‰ to 6‰ and from 1.5‰ to 3.5‰, 539 respectively. Two type I chondrules have very different compositions, NWA 7731 c31 (PO, Mg# ~100), with a host chondrule $\delta^{18}O$ of $-3.56 \pm 0.34\%$ (2SE), δ^{17} 540 O of $-3.86 \pm 0.22\%$ (2SE) and $\Delta^{17}O$ of $-2.01 \pm 0.16\%$ (2SE) and NWA 8649 c27 (PP, Mg#94) with a host chondrule δ^{18} 541 O of $6.76 \pm 0.43\%$ (2SE), $\delta^{17}O$ of $2.57 \pm 0.27\%$ (2SE) and Δ^{17} 542 O of $-0.94 \pm 0.23\%$ (2SE). The

543 petrographic texture of NWA 7731 c31, with pure forsterite olivine and glassy mesostasis, is 544 similar to those of type I PO chondrules with Mg#>99 in Semarkona, that often plot below TFL 545 (e.g., CH44 in Kita et al., 2010; Libourel and Chaussidon, 2011). NWA 8649 c27 is a type I PP 546 chondrule with an unusual texture (Fig. 1e, also see SM2-2) and the oxygen isotope ratios plot on 547 the right side of the PCM line and below the TFL, very close to the CCAM line, which is outside of the range of δ¹⁸O and δ¹⁷ 548 O values that was reported previously by Kita et al. (2010). One type 549 I POP chondrule NWA 7731 c5 plot slightly above the ECL, which is similar to some of the type 550 I POP chondrules in LL3 chondrites determined by Kita et al. (2010). Oxygen isotope ratios of 551 plagioclase-bearing chondrules show a moderate correlation with the anorthite composition as 552 shown in Fig. 8c. Including data from anorthite-bearing chondrules (An>93; Siron et al., 2021), 553 chondrules with higher An compositions plot on or below the TFL. In contrast, chondrules with 554 lower An compositions plot above the TFL, which are similar to glass-bearing chondrules in this 555 work and in the typical range observed from type II chondrules in LL3 (Kita et al., 2010).

In Fig. 9, mass dependent and mass independent fractionations of oxygen isotopes, δ^{18} 556 O and Δ^{17} 557 O, respectively, are compared to the average chondrule Mg#, which are determined as mean 558 Mg# of olivine and pyroxene analyses that were used for the host chondrule computation (see EA1 Table S4). Both δ^{18} O and Δ^{17} 559 O are highly variable for chondrules with high Mg# among type I 560

chondrules (Mg#>90) and converges toward a narrower range for type II chondrules. The mean oxygen isotope signatures of all type II chondrules analyzed in this study are δ^{18} 561 O = 4.9 ± 1.2‰,

 $\delta^{17}O = 3.1 \pm 0.9\%$, and $\Delta^{17} 562~O = 0.50 \pm 0.78\%$ (2SD, n=20), while the mean type II chondrules from L chondrites alone are nearly identical; $\delta^{18}O = 5.0 \pm 1.1\%$, $\delta^{17}O = 3.1 \pm 1.0\%$, and $\Delta^{17} 563~O = 564~0.50 \pm 0.86\%$ (2SD, n=16). These data are very similar to those previously determined for type II chondrules in LL3 chondrites with $\delta^{18}O = 4.5 \pm 0.4\%$, $\delta^{17}O = 2.9 \pm 0.6\%$, and $\Delta^{17} 565~O = 0.54 \pm 0.60\%$ (n=14; Kita et al., 2010). Fig. 9b shows a small but systematic increase of $\Delta^{17} 566~O$ with An 567 compositions of plagioclase as well as correlation between An compositions and chondrule Mg#s. The chondrules studied for Al-Mg chronology in this work have systematically higher $\Delta^{17} 568~O$ than 569 the anorthite-bearing chondrules in UOCs studied by Siron et al. (2021).

570

571 **3.5** Al-Mg isotopes

572 At least 4, but typically 8, spot analyses of plagioclase and/or glass and 4 points of 573 olivine/pyroxene were obtained for each chondrule to construct the Al-Mg isochron regression 574 line. BSE images of the spots after SIMS analyses as well as their location within the chondrules 575 are shown in Supplementary Material SM3. Based on MgO contents of plagioclase and glass by 576 EPMA and their sizes, all plagioclase analyses in NWA 8649 c62 (An₈₇ with 1.0% MgO) and four 577 analyses of glassy mesostasis in QUE 97008 c31 (0.4% MgO) were chosen for SIMS analyses 578 using the FC-EM setting (6 μm spot). Other analyses of glassy mesostasis in QUE 97008 c31 579 (~0.1% MgO) as well as plagioclase and glass in the rest of the chondrules were obtained using 580 the MCEM setting (4 μm spot).

All analyses exhibit excess 581 26 Mg, except glass analyses from two plagioclase-bearing chondrules QUE 97008 c140 and NWA 8276 c43 (Figs. 10-11). Excluding these, the δ 582 26 Mg* 583 values in plagioclase and glass range from 1.4 \pm 0.9% to 142.8 \pm 6.3%. For plagioclase-bearing

chondrules, very high ²⁷Al/ 584 ²⁴Mg ratios (>1,000) are seen among chondrules with An contents of 585 ~10-20%, corresponding to the minimum observed MgO content with respect to plagioclase 586 compositions (Fig. 4b), such as those in NWA 8649 c12 (Ans), QUE 97008 c140 (An6-16) and NWA

8276 c22 (Ans-15). The excess δ 587 ²⁶Mg* in these plagioclase analyses are typically 40-100% with a maximum of 140% (Figs. 10e-f). The measured ²⁷Al/ 588 ²⁴Mg ratios in plagioclase generally decreased with increasing An contents for An>30. The lowest ²⁷Al/ 589 ²⁴Mg ratios of ~30 was obtained 590 in the type I PP chondrule NWA 8649 c62 (Mg# 98), showing eight plagioclase analyses with an indistinguishable excess δ 591 ²⁶Mg* of 1.74 ± 0.35% (2SD) from the MC FC-EM analysis setting

(Fig. 10a). The 27 Al/ 592 24 Mg ratios of glassy mesostasis spots are generally low compared to those in 593 plagioclase with a range of 30-200 (EA1 Table S5-6 and Table 7). Among three glass-bearing 594 chondrules studied, NWA 8276 c59 (Fig. 10b) and NWA 8649 c116 (Fig. 10c) show maximums for their (27 Al/ 24 Mg) of ~80 and ~110, with δ 595 26 Mg* of 4.2 \pm 1.3‰ and 8.0 \pm 1.4‰, respectively.

The third glass-bearing chondrule, QUE 97008 c31 shows a larger range of 27 Al/ 596 24 Mg ratios for the mesostasis analyses, from ~40 to ~190, with δ 597 26 Mg* excess of 2‰ to 10‰, due to the presence 598 of two distinct MgO content areas (~0.4 wt.% and ~0.1 wt.%) within the chondrule (Fig. 10d). As 599 previously mentioned, the two areas were analyzed using two different analytical settings, which

allowed a higher precision from the area with lower 27 Al/ 600 24 Mg ratios. Olivine grains have systematically lower 27 Al/ 24 Mg ratios, between 1.1×10^{-4} and 4.1×10^{-3}

601 , than pyroxene grains, between 2.9×10^{-3} and 2.8×10^{-2} . Their respective δ 602 26 Mg* range between $-0.100\pm0.087\%$ and 603 $0.128\pm0.088\%$ for olivine and between $-0.091\pm0.107\%$ and $0.074\pm0.095\%$ for pyroxene. 604 The results of isochron regression lines for individual chondrules are shown in Figs. 10-11

and summarized in Table 7. All chondrules show correlated $\delta^{26} Mg^*$ excess with their $^{27} Al/$ 605 $^{24} Mg$ ratios, resulting in slopes from 0.0466 \pm 0.0030 to 0.0680 \pm 0.0030 (in the coordinate of δ 606 $^{26} Mg^*$ versus $^{27} Al/^{24} Mg$; Table 7). The intercepts of the regression lines (δ 607 $^{26} Mg^*$)0 are between $-0.051 \pm$ 608 0.048%0 and 0.045 \pm 0.048%0 (2SD), which are generally unresolved from 0 outside their 609

uncertainties. We note that glass analyses in QUE 97008 c140 (Fig. 10f) and NWA 8276 c43 (Fig. 10h) do not show excess δ 610 26 Mg* and are not included in the isochron regressions. The MSWDs 611 for

the regressions are between 0.34 and 1.8. Thus they all represent isochrons for their respective 612 degrees of freedom (Wendt and Carl, 1991). The uncertainty of the slope is smaller for chondrules with high 27 Al/ 613 24 Mg ratios. The two most precise slope determinations are 0.0518 \pm 0.0014 and 614 0.0515 \pm 0.0016 from NWA 8649 c12 and QUE 97008 c140, respectively, that contain albite-rich plagioclase (An~10) with maximum 27 Al/ 24 Mg ratios \geq 2,000 and δ 615 26 Mg* \geq 100%. The 616 uncertainties of these slopes are only ~3% of their values. Similarly, chondrules with Na-rich plagioclase (An<30; with maximum 27 Al/ 617 24 Mg >1,000) show small uncertainties for the slope of 618 their regression lines, corresponding to \leq 6% of their values, while those of the other chondrules are typically smaller than 10%. The final values of inferred (26 Al/ 27 619 Al) $_{0}$ 0 of the chondrules range from (6.5 \pm 0.6)×10 $^{-6}$ to (9.5 \pm 1.0)×10 $^{-6}$

620 (Table 7). These values include propagated uncertainties 621 of RSF (10% for An<30 and glass, 6% for An>30; see section 2.4.4), which typically resulted in ~10% of their values. Exception is NWA 8276 c59 with inferred (26 Al/ 27 Al)0 = (7.7 ± 1.4)×10⁻⁶ 622, which only contains glassy mesostasis with relatively low and restricted ranges of 27 Al/ 623 24 Mg ratios 624 (50-80; Fig. 10b) and has an uncertainty on its slope of ~20%.

The inferred (26 Al/ 27 625 Al)0 are converted to relative ages after CAIs using a canonical value of 5.25×10⁻⁵(Jacobsen et al., 2008; Larsen et al., 2011), with an assumption that 26 626 Al was 627 homogeneously distributed in the early Solar System (e.g., Kita et al., 2013; Budde et al., 2018). The computed ages range from 1.74 ± $^{0.12}$ 628 /0.11 to 2.13 ± 0.09 Ma after CAIs (Table 7). Uncertainties on ages range from ± 0.09 to ± $^{0.20}$ 629 /0.17 Ma. Contrary to what was described in Siron et al. (2021), 630 there is no clear distinction between L and LL chondrite ages, even if the youngest age is found in 631 QUE 97008 (L3.05 chondrite). NWA 8649 c116 (glassy mesostasis chondrule, type II-PP) and NWA 8649 c62 (type I, Mg# = 98) show relatively older Al-Mg ages of 1.74± $^{0.12}$ 632 /0.11 and 1.86 ± $^{0.10}$ 633 /0.09 Ma after CAIs, respectively. Other chondrules show indistinguishable ages range between 1.95 ± $^{0.13}$ 634 /0.11 and 2.13 ± 0.09 Ma after CAIs with a mean of 2.03 ± 0.10 Ma (2SD). When looking at the 6 albite-bearing chondrules (Ans30), they range from 2.00 ± $^{0.11}$ /0.10 to 2.07 ± $^{0.11}$ 635 /0.10 Ma after

636 CAIs.

637

638 4. DISCUSSION

639

640 4.1. Chondrule crystallization

641

642 4.1.1. Crystallization of plagioclase vs glass-bearing chondrule

chondrules compared to glass-bearing chondrules is very important since plagioclase-bearing chondrules are a good target for 26 Al 26 Mg dating due to their high 27 Al/ 24 Mg ratios and δ 645 26 Mg*. 646 It has been recently shown that about 20% of chondrules in UOCs have plagioclase as their main 647 mesostasis phase (Lewis and Jones, 2019). In their paper they show that plagioclase is a primary 648 product of melt crystallization and only contains minor amount of clay minerals, located at the 649 grain boundary. From the petrography of the selected chondrules, it is clear that olivine and 650 pyroxene textures are very similar, whether they have glass or plagioclase as the main mesostasis 651 phase. Typical type II PO are usually glass-bearing chondrules, but here, MET 00452 c85 has 652 plagioclase grains as the main mesostasis phase while having the same texture for olivine 653 phenocrysts (Fig. 2f) and small low-Ca pyroxene (Fig. 3b). Additionally, the plagioclase is a pure 654 albite (An₃) and glass for these types of chondrule usually have very low CaO and high Na2O 655 contents. Similarly, plagioclase-bearing type II POP chondrules, whether they are mineralogically 656 zoned or not, have very similar textures for olivine and pyroxenes than glass-bearing chondrules. 657 Olivine chadacrysts inside low-Ca pyroxenes and olivine phenocrysts, elongated or not, that show 658 typical zoning toward the edge, can be found in plagioclase-bearing chondrules such as QUE 659 97008 c140 (Fig. 2d) or Semarkona c55 (Fig. 2e) or glass-bearing chondrules such as NWA 7731 660 c52 (Fig. 3e). When taking a closer look, one cannot distinguish these two populations of 661 chondrules when only looking at their olivine and pyroxene textures, as highlighted in Figs 2-3, 662 where Semarkona c55 (Fig. 3d) is extremely similar to NWA 7731 c52 (Fig. 3e).

643 Understanding the difference in terms of crystallization history of plagioclase-bearing 644

663 Experiments have shown that plagioclase crystallizes at the later stage under slower 664 cooling

rates of the order of 1-10 °C/h (Tronche et al., 2007; Rocha and Jones, 2012; Wick and 665 Jones, 2012), while glass is found in faster cooling rate experiments of the order of 100 °C/h 666 (Lofgren, 1989; Jones and Lofgren, 1993). Nevertheless, even for plagioclase-bearing chondrules, 667 slow cooling rates might not be the case throughout the entire crystallization of the chondrule and 668 only be representative of the end of crystallization.

669 One striking difference between plagioclase- and glass-bearing chondrules are their K₂O 670 content. In the case of plagioclase, due to their very low K2O content, no K2O bearing phase can 671 be found in the chondrule, while glass has between 0.8-1.4 wt.% K₂O. TEM sections from Lewis 672 and Jones (2019) showed that no K₂O enrichment in plagioclase can be found at the boundary 673 between plagioclase grains or plagioclase and glass. Although some chondrules have glass area 674 that most likely represent residual melt pockets, most plagioclase-bearing chondrules are entirely 675 crystallized, and thus, free of any K₂O bearing phase. We consider two hypotheses that can explain 676 this feature. (1) Chondrule melt was originally depleted in K2O relative to Na2O, so that primary 677 chondrule glassy mesostasis were depleted in K2O, as in plagioclase. Additional K2O diffused into 678 the chondrule mesostasis after crystallization, either during aqueous alteration in their parent body 679 (Grossman et al., 2000) or due to terrestrial weathering. (2) Chondrule melt was abundant in both 680 Na₂O and K₂O and were retained in chondrules with glassy mesostasis, though K₂O was lost from 681 chondrules with plagioclase-bearing mesostasis where Na₂O was retained in plagioclase. 682 The problem with the first hypothesis is the slower self-diffusion of K2O compare to Na2O 683 in glass (Guo and Zhang, 2016), even if the melt composition of these experiments was more 684 basaltic and is not completely representative of type II chondrule mesostasis composition. If K2O 685 was introduced in glass by diffusion, Na₂O content should not be consistent between glass and 686 olivine, which has been demonstrated to be the case (Alexander et al., 2008). Nevertheless, the 687 zoning of K₂O observed in Pape et al. (2021) with higher K₂O content in the rim of a chondrule in 688 MET 00452 (labelled as Ch22) and generally increasing K₂O content toward the rim, from 0.4 689 wt.% in the inner part to 1.4 wt.% in the outer part of the chondrule, would be consistent with K2O 690 diffusion from the exterior of the chondrule. This was argued for several zoned chondrules from 691 Semarkona by Grossman et al. (2002), who interpreted this as the consequence of low 692 temperature aqueous alteration in the parent body. In the case of the second hypothesis, 693 chondrules with glassy mesostasis cooled fast and

retained both Na₂O and K₂O against evaporation 694 under high dust density (e.g., Alexander et al., 2008). In contrast, chondrules with plagioclase 695 cooled slowly, in which K₂O concentrated in melt due to smaller plagioclase/melt partition 696 coefficient than Na₂O (Dohmen and Blundy, 2014). During the slow cooling, K₂O in melt had 697 evaporated from chondrule melt before mesostasis solidified completely into plagioclase and high 698 Ca pyroxene. Therefore, we suggest that the second hypothesis, loss of K₂O from the mesostasis 699 during plagioclase crystallization, is probably preferable.

700

701 **4.2 Oxygen isotopes signatures**

702

703 It is widely accepted that L and LL chondrites come from different parent bodies with 704 different bulk siderophile elements and mineral compositions (e.g., Brearley and Jones, 1999). 705 Bulk oxygen isotope ratios of equilibrated L and LL chondrites show a systematic difference along 706 the slope 1.0 line (Clayton et al., 1991). Chondrule oxygen three-isotope signatures are influenced 707 by the local composition of solid precursors in the proto-planetary disk and the ambient gas during 708 transient melting event (Kita et al., 2010). In this study, we obtained oxygen isotope ratios of 21 709 chondrules from L chondrites, which are generally indistinguishable from the 4 chondrules from

710 LL chondrite chondrules from this study as well as those of Kita et al. (2010). This indicates that 711 the formation of chondrules in L and LL chondrites occurred in regions composed of solid 712 precursors with common oxygen isotope ratios, but having different local abundance of metal and 713 siderophile elements.

714 New data from this study including chondrules in both L, LL, and MET 00452 (L(LL)) show variations of δ^{18} O and Δ^{17} 715 O against Mg# that are very similar to those previously reported in LL3 chondrite chondrules by Kita et al. (2010) (Fig. 9). In Fig. 9, both δ^{18} O and Δ^{17} 716 O values 717 are highly variable for high Mg# (i.e., > 95%) chondrules and converge to a small range with 718 decreasing Mg#. This indicates that precursors of ordinary chondrite chondrules might have contained (1) 16 O-poor precursors with Δ^{17} O >1.6‰ and (2) 16 719 O-rich precursors similar to those 720 of carbonaceous chondrites (Kita et al., 2010). There could have been a mass dependent fractionation process that occurred for 16 721 O-poor precursors of type I chondrules in the solar nebula 722 prior to chondrule

formation or during type I chondrule formation under an open system behavior 723 for major oxide between chondrule melt and ambient gas (Nagahara et al., 2008), which resulted in lower δ^{18} 724 O in type I PO chondrules (Kita et al., 2010). Locally, as the dust density in chondrule 725 forming regions had increased, Mg# of chondrules decreased and oxygen isotope ratios were more

726 homogenized to show a smaller range of variations. Systematic changes in An compositions of 727 plagioclase with chondrule Mg# among chondrules studied here (Fig. 4a and Fig. 9) indicate that 728 chondrules formed with higher alkali element abundances with increase of local dust density. As 729 shown in Fig. 9b, plagioclase-bearing chondrules with higher An contents (An>50) tend to show lower Δ^{17} 730 O. This is also seen clearly from anorthite-bearing chondrules studied by Siron et al. 731 (2021) compared those with lower An compositions (An<50) from this study. These data probably indicate that the contribution of refractory-rich (Na-poor) and 16 732 O-rich precursors were variable 733 among chondrules with different An compositions.

734

735

736 4.3 Parent body thermal metamorphism effect on Al-Mg ages

737

738 Several observations point towards a limited effect of parent body thermal metamorphism on the ²⁶Al- 739 ²⁶Mg ages determined in this study: 1) the chondrites selected are among the least 740 affected by parent body metamorphism (3.00-3.05), as determined by Cr₂O₃ contents in olivine by 741 methods described in Grossmann and Brearley (2005). 2) The additional assessment of subtypes 742 from Fe-Ni metal presented here confirm that these selected chondrites are similar to low subtypes 743 3.05-3.10, except for Semarkona being 3.00 (or 3.01 by Kimura et al., 2008) and the most pristine UOC studied here. 3) All ²⁶Al- 744 ²⁶Mg isochrons for the studied chondrules gave well-correlated 745 linear trend with reasonable MSWDs (i.e., close to 1). 4) Mg self-diffusion to reset a 10 μm diameter sphere of albite of one half-life (0.7 Ma; i.e., 50% loss of excess 746 ²⁶Mg) would require 6 747 Ga at 300 °C (Van Orman et al., 2014). Semarkona is known to have never experienced 748 temperatures higher than 260 °C (Alexander et al., 1989), which makes it impossible for Al-Mg

749 systematics of plagioclase to be significantly modified during parent body metamorphism. For 750

chondrules in other meteorites with low subtypes (~3.05), they probably never experienced 751 temperature higher than 500 °C (Kimura et al., 2008). At such temperatures, it would require only 752 1 ka to reset of one half-life a 10 µm diameter sphere of albitic composition. Such a fast process 753 would not be resolvable with the current analytical method so that variations observed among 754 chondrule ages might also represent small variations of metamorphism between chondrules. 755 Nevertheless, analyses of albitic plagioclase that located extremely close to one another yield very

different 27 Al/ 24 Mg ratios and excess 756 26 Mg as shown in Fig. 12 for QUE 97008 c140 (Fig. 12a; 757 An₆₋₁₆) and NWA 8649 c12 (Fig. 12b; An₈), while they plot on a single isochron regression line 758 along with other data points. QUE 97008 c140 shows two analyses at ~10 µm from one another with 27 Al/ 24 Mg of 572 ± 10 (2SE) and 731 ± 29 (2SE) and δ 759 26 Mg* of 29.8 ± 2.8% (2SE) and 39.4 760 ± 3.3% (2SE), respectively. Even more compelling, NWA 8649 c12 has three analyses each at 10

 μ m distance from the other with 27 Al/ 761 24 Mg of 1358 \pm 23 (2SE), 1194 \pm 13 (2SE) and 2347 \pm 24 (2SE) and δ 762 26 Mg* of 72.2 \pm 4.1% $_{o}$ (2SE), 63.8 \pm 4.0% $_{o}$ (2SE) and 122.1 \pm 6.1% $_{o}$ (2SE), 763 respectively. The fact that analyses at 10 μ m distance from one another yield a consistent

relationship between 27 Al/ 24 Mg ratios and excess 764 26 Mg with results that differ outside of their uncertainties for both 27 Al/ 24 Mg and δ 765 26 Mg* is a good evidence that even albitic plagioclase grains 766 of chondrules from ~3.05 chondrites did not show re-equilibration of their Al-Mg isotopes. 767 The use of excess silica to evaluate the degree of parent body metamorphism is subject to 768 caution when considering more albitic plagioclase since it is very clear that its Ca-Na composition 769 exerts a strong control on the excess silica incorporation (Fig. 4c). Plagioclases with An₂₀₋₅₀ do not 770 show any excess silica, this is very troubling and is most probably the consequence of a 771 crystallographic control

rather than being due to selective parent body metamorphism that would

772 anneal the primary excess silica signature only for this compositional range. However, for higher 773 anorthite content, it seems that excess silica is a good indicator to look at to estimate the degree of 774 parent body metamorphism, as previously highlighted (Tenner et al., 2019). 775 While there is no indication for disturbance in the Al-Mg chronometer of plagioclase 776 among the studied chondrules, two chondrules QUE 97008 c140 and NWA 8276 c43 show glass

analyses that do not show resolvable excess δ 777 26 Mg* and are off the isochron regression lines 778 defined by plagioclase analyses of the same chondrules. These glass analyses may represent 779 disturbance of Al-Mg system due to low degree thermal metamorphism in type \sim 3.05 chondrites. 780 However, the effect seems to be selective to specific chondrules because other glass-bearing 781 chondrules, including two in the same meteorites QUE 97008 and NWA 8276, show resolvable

 δ 782 26 Mg* and good isochron regression lines. Another chondrules NWA 8649 c27 show one analysis 783 of glass that plot on the isochron defined by plagioclase analyses. It is clear from these data that 784 the Al-Mg chronometer in glassy mesostasis is more sensitive to parent body thermal 785 metamorphism than in plagioclase crystals.

786

787 4.4 Parent body aqueous alteration and terrestrial weathering effect on Al-Mg ages

788

789 As described in the petrographic description, the studied chondrules are all affected by 790 various amount of terrestrial weathering and most of them show evidences of limited aqueous 791 alteration inside the parent body. As for all secondary processes, terrestrial weathering or aqueous 792 alteration could either affect the quality of the isochron by locally modifying the Al-Mg 793 composition and increasing the scatter of the data around the isochron and/or modify the Al-Mg 794 age. The first should result in higher MSWDs for chondrules that are highly affected by aqueous

795 alteration or weathering. The latter should be visible when comparing chondrules ages with 796 different degrees of aqueous alteration or weathering. The impact of both terrestrial weathering 797 and aqueous alteration are discussed together in this section since it is not always easy to clearly 798 ascribe alteration features to one or the other. For example, Fe-Ni metal blobs alteration to Fe

799 oxide or hydroxide and sulfide can be the result of both processes (Lee and Bland, 2004). 800 The two chondrules that are the most 37ffectted by terrestrial weathering are NWA 8649 801 c27 and c62. Thus, if this process significantly affects the Al-Mg chronology, these two chondrules 802 should be the most affected. NWA 8649 c27 and c62 have a MSWD of 0.84 (p-value of 0.56) and 803 0.36 (p-value of 0.96), respectively. Although NWA 8649 c62 has a MSWD slightly lower than 804 what would be

expected for a degree of freedom of 10, they both clearly do not exhibit a higher 805 scattering of individual Al-Mg analyses than the rest of the chondrules. Similarly, with an Al-Mg age after CAIs of $1.98 \pm 0.12/0.11$ Ma and 1.86 ± 0.10 806 /0.09 Ma, for NWA 8649 c27 and c62, 807 respectively, they both are within the range of Al-Mg ages of the rest of the chondrules. 808 It is important to note that the studied plagioclase-bearing chondrules do not show 809 replacement of primary plagioclase by secondary minerals, e.g., sodalite, nepheline or clay 810 minerals, or modification of their composition with increasing orthoclase component as is the case 811 for strongly affected chondrules (Lewis et al., 2022). NWA 7731 c33, NWA 8276 c22 and c43 812 (Fig. 3f) have small glass areas that are partially leached or altered. On the opposite, NWA 8649 813 c27 still has fresh glass areas between plagioclase grains. These potentially affected chondrules 814 have MSWDs between 0.34 (p-value of 0.97) and 1.4 (p-value of 0.17) and the Al-Mg ages range from $2.01 \pm 0.11/0.10$ Ma to 2.07 ± 0.13 815 /0.11 Ma, which are not resolved from the rest of the dated 816 chondrules.

817 Based on this dataset, it seems that both aqueous alteration and weathering do not affect 818 the determination of Al-Mg ages in chondrules, at least at the level of precision of ±0.1 Ma. It 819 cannot be excluded that it resulted in some minor additional scattering within the small range of 820 ages determined here. An important factor to consider though is that, in this study, we carefully 821 selected the areas to analyze in order to avoid any grain boundary or terrestrial weathering product 822 such as Fe-rich veins. When another mineral was hit during an individual analysis, the affected 823 cycles were excluded from the analysis. This is important since weathering or aqueous alteration 824 are processes that affect more the grain boundaries than the interior of grains (Lewis and Jones, 825 2019). Indeed, dissolution of glass always start at the boundary between glass and plagioclase or 826 mafic minerals and some weathering can be seen between olivine chadacrysts and their pyroxene 827 host.

828

829 4.5 Discrepancy between datasets on Al-Mg ages

830

831 Figure 13a shows the total range of ages determined for plagioclase- or glass-bearing 832 chondrules in this study, along with those of anorthite-bearing chondrules reported in Siron et al. 833 (2021). There is no relationship between the relative age and the chondrule type (Fig. 13a) nor the 834

anorthite content for these chondrules (Fig. 13b). This range of ~0.4 Ma is also very similar to 835 what was found in Siron et al. (2021) for 14 anorthite-bearing chondrules, with Mg# spanning a 836 range of 76-97 mole%. It seems that, overall, most of the anorthite-bearing chondrules are slightly 837 older than their Na-rich counterpart, especially visible on the density map from Fig. 13b. This is 838 confirmed by the kernel density estimates (Fig. 14a) where anorthite-bearing chondrules (Siron et 839 al. 2021) and plagioclase-bearing chondrules from this study are compared. There is a small peak 840 with older Al-Mg age for plagioclase-bearing chondrule from this study, which represent the 841 slightly older age of NWA 8649 c62 that has plagioclase grains with a composition of Ans7. This 842 difference is very small (0.1-0.15 Ma) and is in the same order of magnitude than the uncertainty 843 assigned to RSF for Na-rich plagioclase and glass where no matrix matching standards with well

calibrated reference value for the ²⁷Al/ 844 ²⁴Mg ratio are available. Nevertheless, this highlights the 845 need for very precise ages, i.e., ~0.1 Ma, for future studies in order to confirm whether we can 846 distinguish multiple chondrule forming events using the Al-Mg chronometer. 847 In the following paragraphs, we compare Al-Mg data of UOC chondrules that were 848 obtained from large radius SIMS analyses (Kita et al. 2000; Villeneuve et al. 2009; Bollard et al. 849 2019; Pape et al. 2019; Siron et al. 2021; this study). We do not include data from Mostefaoui et 850 al. (2002) that analyzed slightly metamorphosed UOC Bishunpur (LL 3.15; Grossman and 851 Brearley, 2005). To be able to compare relative Al-Mg ages consistently among different studies, the inferred initial (²⁶Al/²⁷ 852 Al)₀ of UOC chondrules from these earlier studies were converted to relative ages using the same canonical $(^{26}\text{Al}/^{27}\text{Al})_0$ of 5.25×10^{-5} for CAIs and half-life of 26 853 Al 854 (0.705 Ma) as in this study and Siron et al. (2021). Kita et al. (2000) dated 3 plagioclase-bearing 855 chondrules and 2 glass-bearing chondrules from Semarkona, while Bollard et al. (2019) dated 6 856 plagioclase-bearing chondrules and 2 glass-bearing chondrules from NWA 5697 (L3.10). As 857 mentioned above, Siron et al. (2021) dated 14 anorthite-bearing chondrules. Even if the individual 858 uncertainties for Kita et al. (2000) and Bollard et al. (2019) were larger due to the use of a single collector EM, they obtained inferred $(^{26}\text{Al}/^{27}\text{Al})_0$ between $(5.7 \pm 2.6) \times 10^{-6}$ and $(9.2 \pm 5.0) \times 10^{-6}$ 859 and between $(4.5 \pm 1.1) \times 10^{-6}$ and $(8.9 \pm 1.1) \times 10^{-6}$ $1.8) \times 10^{-6}$

860 , respectively. This corresponds to age ranges between 1.8 \pm $^{0.8}$ /0.4 Ma and 2.3 \pm $^{0.6}$ /0.4 Ma and

between 1.81 \pm $^{0.24}$ /0.19 Ma and 2.51 \pm $^{0.28}$ 861 /0.22 Ma, 862 for Kita et al. (2000) and Bollard et al. (2019), respectively. Villeneuve et al. (2009) determined

inferred (26 Al/ 27 Al)0 from (3.0 ± 1.2)×10⁻⁶to (1.62 ± 0.17)×10⁻⁵ 863 from 14 glass-bearing chondrules from Semarkona (LL3.00), with a peak at ~7×10⁻⁶

864 . This corresponds to relative ages between 1.2 \pm 0.1 Ma to 2.9 \pm ^{0.5} 865 /0.3 Ma with a peak at ~2.0 Ma after CAIs. Pape et al. (2019) determined inferred (26 AI/ 27 AI)0 from (3.1 \pm 1.2)×10⁻⁶ to (9.5 \pm 2.8)×10⁻⁶

866 from 30 glass-bearing chondrules from several different UOCs with two peaks at $\sim 7.5 \times 10^{-6}$ and $\sim 5.5 \times 10^{-6}$

867 , corresponding to relative ages from 1.7 ± 0.3 Ma to $2.9 \pm {}^{0.5}$ 868 /0.3 Ma with two peaks at ~2.0 Ma and ~2.3 Ma after CAIs. Kita 869 et al. (2000), Bollard et al. (2019), Siron et al. (2021), and this study have in common the use of 870 small primary beam spots to avoid overlap between mesostasis and mafic minerals, as well as 871 having analyzed mostly plagioclase-bearing chondrules. On the contrary, Villeneuve et al. (2009) 872 and Pape et al. (2019) used high precision SIMS MCFC analyses with large and intense primary 873 beam (30-40 μ m) that often resulted in mixed analyses of mesostasis and high-Ca pyroxene micro

874 crystallites and only dated glass-bearing chondrules. The discrepancy in terms of duration for 875 chondrule ages between small and large spots methodologies is particularly visible on Fig. 14b, 876 where the kernel density estimates for data from large spots studies (red) span a much wider range 877 than the data for small spots studies (blue). Here we do not use the widely used probability density 878 function (PDF) since it lacks any theoretical basis and can produce counter-intuitive results 879 (Vermeesch, 2012), especially since here the analytical uncertainties are very different between 880 the different studies.

881 There are four main hypotheses to explain discrepancy in Al-Mg ages between small and 882 large spot analyses, 1) there is a sampling bias in the dated chondrules since most chondrules from 883 small spots studies are plagioclase-bearing chondrules while large spots studies only analyzed 884 glass-bearing chondrules; 2) glass-bearing chondrules are more affected by secondary processes 885 and the larger age variations are due to variations in metamorphism or aqueous alteration; 3) the

886 mixing of glass and high-Ca pyroxene grains for some analyses from large spot studies introduces 887 a bias due to a difference in sputtering and extraction of secondary ions during SIMS analyses; 4) a small inaccuracy of δ 888 ²⁶Mg* in mesostasis analyses (~0.07‰) from large spot studies that are comparable to their small 889 ²⁶Mg excesses.

890 The first hypothesis is easy to assess since all small spot studies, except Siron et al. (2021), 891 analyzed at least one glass-bearing chondrule. Kita et al. (2000) analyzed two glass-bearing 892 chondrules and three plagioclase-bearing chondrules. Ages from two glass-bearing chondrules, 893 i.e., 1.8 ± 0.2 Ma and 2.1 ± 0.3 Ma, yielded indistinguishable ages from the three plagioclase bearing chondrules, i.e., $1.8 \pm 0.4/0.3$ Ma, $1.8 \pm 0.8/0.4$ Ma and $2.3 \pm 0.6/0.4$ Ma. Bollard et al. (2019) analyzed one glass-bearing chondrules that yielded an age of $1.90 \pm 0.42895 /0.30$ Ma and six plagioclase bearing chondrules with ages between 1.81 \pm 0.24/0.19 Ma and 2.51 \pm 0.28 896 /0.22 Ma. Again, the glass 897 bearing chondrule age is indistinguishable from the plagioclase-bearing chondrule ages. In the 898 present study, three glass-bearing chondrules and 14 plagioclase-bearing chondrules yield ages range between $1.74 \pm \frac{0.11}{0.12}$ Ma and $1.94 \pm \frac{0.20}{0.17}$ Ma for the first and between $1.86 \pm \frac{0.09}{0.19}$ 899 /0.10 Ma 900 and 2.13 ± 0.09 Ma for the latter. Again, ages from glass-bearing and plagioclase-bearing 901 chondrules are indistinguishable. When taking together, small spot studies have analyzed 6 glass 902 bearing chondrules and 37 plagioclase-bearing chondrules. Although it is clear that the dataset of 903 this study is skewed towards plagioclase-bearing chondrules and thus the age distribution of the 904 latter is better constrained than the first, all 6 glass-bearing chondrules from small spots analyses 905 exhibit the same age range than plagioclase-bearing chondrules.

906 One argument in favor of the second hypothesis is the fact that two plagioclase-bearing chondrules in this study exhibited well-correlated excess 907 ²⁶Mg for plagioclase analyses but not for 908 glass analyses. This confirm that glass is more sensitive to secondary processes than plagioclase 909 and that the latter will preserve pristine Al-Mg isochron better than the former. Indeed, in both 910 Villeneuve et al. (2009) and Pape et al. (2019), one chondrule exhibited a negative or flat fit for 911 multiple Al-Mg analyses, even if it didn't represent the chondrule with the lowest number of

individual analyses or lowest ²⁷Al/ 912 ²⁴Mg ratios, excluding that this was purely a statistical

913 fluctuation. No explanation was given as of why these chondrules were different from the rest of the chondrules analyzed. One chondrule showing a younger age of $2.88 \pm {}^{0.74}$ 914 /0.42 Ma show a glass 915 compositional zoning in CaO, Na₂O, K₂O and SiO₂ from core to rim of the chondrule which was 916 later interpreted as remelting (Pape et al., 2021). However, this zoning is similar to what was 917 described by Grossman et al. (2002) as parent body aqueous alteration for chondrules from 918 Semarkona. Indeed, even with the absence of devitrification of glass, Grossman et al. (2002) 919 showed that aqueous alteration promotes the replacement of the primary glass composition, which could have disturbed Al-Mg chronology. The distribution of inferred (26 Al/ 27 920 Al)₀ shifted more to lower values (peak at 5.5×10^{-6}

921) in Pape et al. (2019) than those in Villeneuve et al. (2009) with a peak at 7×10^{-6}

922 , which may be attributed to systematic difference in the degree of thermal 923 metamorphism experienced by chondrules used in these studies. Villeneuve et al. (2009) studied 924 chondrules only from Semarkona (LL3.00), the least metamorphosed UOC, while all chondrules 925 studied by Pape et al. (2019) were from UOCs with subtypes 3.05-3.15, including NWA 8276 that 926 is considered to be a pair with NWA 7731, both of which were originally classified as L3.00 from 927 Cr₂O₃ in olivine (Agee et al., 2013; Ruzicka et al., 2017), but chemistry and texture of Fe-Ni metal 928 in this study indicate that they are in fact subtypes 3.05-3.10.

In order to take into account the difference in ²⁷Al/ 929 ²⁴Mg ratios and precision of Mg isotope 930 analyses between the two methodologies, a better measure of the potential disturbance in Al-Mg 931 chronometer is the MSWD values of isochron regression lines. Indeed, to evaluate the statistical

932 significance of regression lines obtained for isochrons, the MSWD has long been the mathematical 933 function chosen. The importance of using the MSWD to interpret the significance of initial ratios has been highlighted again recently for ¹⁰Be/⁹

934 Be initial ratios (Dunham et al., 2020). Of the 31 935 chondrules analyzed by Siron et al. (2021) and this study, only two have a MSWD that would 936 consider them as an errorchron (Wendt and Carl, 1991), with MSWDs at 2.1 and 1.8. On the other

hand, 5 out of 14 chondrules with excess $937^{26}Mg$ for Villeneuve et al. (2009) and 7 out of 30

938 chondrules for Pape et al. (2019) are errorchrons and not isochrons. Such a high ratio of errorchrons 939 could be either due to the analytical setting chosen or later disturbance of the chronometer. 940 Alexander and Ebel (2012) argued for variable degrees of disturbance during parent body 941 alteration to explain the range of ages from Villeneuve et al. (2009). If any small degrees of thermal 942 metamorphism in addition to aqueous alteration took part in these chondrules, due to faster grain 943 boundary diffusion and preferential pathways for fluids, small amount of diffusion or alteration 944 would be more easily achieved at the grain boundary. Chondrules containing large (>30 µm) 945 domain of clean mesostasis are rare, so that most chondrules selected for large spot analyses 946 contain abundant micro-crystallites set in glassy mesostasis (Pape et al. 2019). This could explain 947 why these two studies where at least some spots consisted of a mix of glass and high-Ca pyroxene, 948 and thus the grain boundary in-between, show an abnormal amount of errorchrons. Avoiding the 949 grain boundary by selecting areas large enough to locate a SIMS analysis, as is the case for small 950 spot studies, may allow to avoid this pitfall.

951 The high number of errorchrons in both Villeneuve et al. (2009) and Pape et al. (2019) 952 could also be due to a discontinuity of sputtering and extraction of secondary ions implied by the 953 grain boundary for mixed glass and high-Ca pyroxene analyses (hypothesis 3). Although there is 954 no clear difference in RSF between glass and pyroxene when analyzed separately, this is not the 955 case when both are mixed inside a SIMS analysis. Here the analytical conditions are not the same 956 anymore and the grain boundary might disrupt the sputtering and extraction of ions. This is 957 especially concerning since Pape et al. (2019) show that fractures result in Al-Mg analyses with

lower excess 958 26 Mg. Additionally, in the same example (Fig. 3 of their paper), the spot that represent a mix of glass and high-Ca pyroxene also has a lower δ 959 26 Mg* than the rest of the spots for this 960 chondrule. Although the value is within error of the isochron, there seem to be a general trend that 961 any disruption of the analyses tends to give younger Al-Mg systematics. There are no SIMS pits 962 images available for all chondrules studied by Villeneuve et al. (2009) and Pape et al. (2019), so 963 that there is no way to know the frequency of mixed analyses and how they affected isochron 964 regression lines. A direct comparison would need to be made between the same chondrule

analyzed 965 with the two different methods to demonstrate whether the difference in timescale between these 966 two methods is due to parent body alteration of glassy mesostasis or mixing of glass and high-Ca 967 pyroxene grains.

968 The last hypothesis to explain the discrepancy between large and small spot studies is the fact that most chondrules analyzed by large spot studies have low ²⁷Al/ 969 ²⁴Mg ratios for their 970 mesostasis analyses while small spot studies mostly target chondrules with mesostasis having high ²⁷Al/²⁴Mg ratios. High ²⁷Al/ 971 ²⁴Mg ratios usually involves analyzing low Mg contents and thus a bigger uncertainty on 5 972 ²⁶Mg* since the biggest contribution to the final uncertainty is the counting statistics of individual measurements. This is not the case for low ²⁷Al/ 973 ²⁴Mg ratios, where small δ 974 ²⁶Mg* are more heavily impacted by systematic uncertainties, such as the calibration of excess 975 ²⁶Mg using terrestrial standards, or external reproducibility that are estimated from repeated 976 analyses of multiple standards (typically 0.04%e-0.06%e). Villeneuve et al. (2009) and Pape et al. (2019) have analyzed mainly low

chondrules having their highest ²⁷Al/ 978 ²⁴Mg lower than 10. At these levels, even a 0.05‰ uncertainty on the calibration of excess ²⁶Mg can heavily influence the determination of the (²⁶Al/²⁷ 979 Al)₀. This is particularly visible on Fig. 15, where the highest measured ²⁷Al/ 980 ²⁴Mg analysis for each chondrule is plotted against the inferred (²⁶Al/²⁷Al)₀. The variations of inferred (²⁶Al/²⁷ 981 Al)₀, and thus chondrule ages after CAIs, is much higher at lower ²⁷Al/ 982 ²⁴Mg. In fact, for both studies, all chondrules that contain mesostasis analyses with a ²⁷Al/ 983 ²⁴Mg higher than 15 exhibit an inferred (²⁶Al/²⁷Al)₀ in agreement, within error, with the (6-9)×10⁻⁶

984 range determined for this study and 985 Siron et al. (2021).

986 Alternatively, an additional explanation for this disparity would be that the younger ages 987 found in Villeneuve et al. (2009) and Pape et al. (2019) are due to partial remelting events, as 988 demonstrated by Pape et al. (2021) for one of MET 00452 chondrules dated by Pape et al. (2019) 989 (Pape et al., 2021). However, of the 43 chondrules dated using small primary beams (Kita et al., 990 2000; Siron et al., 2021), not a single one exhibit a younger age that could be linked to a remelting 991 event. The only feature in this study that could be potentially linked to a remelting event is the 992 zoned plagioclase in

NWA 8649 c27 (Fig. 1e), showing a sharp transition between a core (An₇₀) 993 and rim (An₅₈) compositions. Additionally, this chondrule has a very particular oxygen three 994 composition for the pyroxene phenocryst (Fig. 6a). Nevertheless, this chondrule has an inferred (26 Al/ 27 Al)₀ of (7.5 ± 0.9)×10⁻⁶, which corresponds to an age of 1.98 ± $^{0.13}$ 995 /_{0.11} Ma after CAIs and 996 the boundary between the two zones in the large plagioclase grain is parallel to the external faces 997 of the grains which makes it hard to believe that this represent a remelting of an original grain. 998 This most likely represent a two stages growth of plagioclase during primary crystallization. This 999 makes it hard to imagine that all remelted chondrules would have been dated through the large 1000 spot method of Villeneuve et al. (2009) and Pape et al. (2019).

1001 As shown in the discussion above, it is hard to decipher the reason(s) of the discrepancy 1002 between small and large spot studies. It might even not be a single reason but a combination of 1003 several reasons. Nevertheless, in our opinion, the most likely explanation for the discrepancy 1004 between the two datasets is the fact that glass is more prone to alteration during secondary 1005 processes than plagioclase. Thus, we believe that the range observed in this study and in Siron et 1006 al. (2021) represent the true range of UOC chondrule formation.

1007

1008

1009 **4.6 Timing for chondrule formation**

1010

Based on the ²⁶Al- 1011 ²⁶Mg ages determined in this study, there is no resolvable difference 1012 observed between chondrule ages from L and LL chondrites (Fig. 13a). This is in contradiction to 1013 what was found in Siron et al. (2021), where all younger anorthite-bearing chondrules were from 1014 L chondrites. Nevertheless, the 5 younger chondrules from QUE 97008 and NWA 8276, both L 1015 chondrites, have ages ranging from 2.00 to 2.16 Ma after CAIs, which is similar to Na-rich 1016 chondrules presented here. Since Siron et al. (2021) concluded that these unusual, alkali-depleted, 1017 anorthite-bearing chondrules probably formed in a less dense environment than typical Na-rich 1018 chondrules such as those studied here, the different chondrule forming events at ~1.9 Ma and ~2.0 1019 Ma after CAIs might have either happened in different forming regions of the

protoplanetary disk 1020 or represent a densification of the dust in the disk. Since very dense environments should lead to 1021 the formation of parent bodies very quickly after the chondrule forming process ends (Alexander 1022 et al., 2008; Alexander and Ebel, 2012), most anorthite-bearing chondrules might have formed 1023 earlier in a slightly less dense environment and be sampled into the different parent bodies quickly

1024 after Na-rich chondrules formed in a dense environment. Nevertheless, since there are 5 anorthite 1025 bearing chondrules with ages younger than 2.0 Ma after CAIs, they would have been formed 1026 concomitantly to the Na-rich chondrules from this study. Thus, both hypotheses require at least 1027 some degree of dust density heterogeneity in the disk.

When considering plagioclase only, the range of $(^{26}\text{Al}/^{27}\ 1028\ \text{Al})_0$ determined in this study is between $(6.5 \pm 0.6) \times 10^{-6}$ and $(8.5 \pm 0.8) \times 10^{-6}$

1029 , with all plagioclase with An < 60 being between $(6.5 \pm 0.6) \times 10^{-6}$ and $(7.5 \pm 0.9) \times 10^{-6}$. This corresponds to ages ranging between $1.86 \pm {}^{0.10}$ 1030 /0.09 and 2.13 ± 0.09 (2SD) Ma after CAIs for all plagioclases and between $1.98 \pm {}^{0.13}$ 1031 /0.11 and 2.13 ± 0.09 1032 (2SD) for An < 60. The major chondrule forming event would then be located at ~2.00 Ma after 1033 CAIs and be followed very rapidly by the aggregation into a large parent body (Desch et al., 2018; 1034 Edwards and Blackburn, 2020). Such short timescale for chondrule formation is in very good 1035 agreement with Alexander et al. (2008), and implies a very high dust density, at least in the 1036 chondrule forming region of type II Na-rich chondrules.

1037 Since no rhyolitic glass standards were used in this study, the difference in matrix effect and ²⁷Al/ 1038 ²⁴Mg RSF between the anorthite glass and labradorite mineral standards and the glass 1039 analyzed in this study cannot be constrained. The additional 10% error added to the error on the 1040 slope is a systematic error and can only be seen as an attempt to evaluate this additional uncertainty. 1041 Interestingly, two glass-bearing chondrules, QUE 97008 c31 and NWA 8276 c59, have very similar ages, 1.95 ± ^{0.13}/_{0.11} and 1.96 ± ^{0.20} 1042 /_{0.17} Ma after CAIs, respectively. Yet, they have different 1043 Na₂O content, ~8 and 5 wt.%, respectively, and different FeO content, ~4-5 and 10 wt.%, 1044 respectively. While the third glass-bearing chondrule, NWA 8649 c116, has a slightly older age of 1.74 ± ^{0.12} 1045 /_{0.11} Ma, but has Na₂O contents of ~10 wt.% and FeO contents of ~4 wt.%, both of which 1046 are very

similar to those for QUE 97008 c31. Thus, it is unlikely that the age difference between

1047 QUE 97008 c31 and NWA 8276 c59 at ~1.95 Ma and NWA 8649 c116 at ~1.75 Ma is the result 1048 of a difference in matrix effect due to Na2O or FeO contents. It is worth noting that this chondrule 1049 has the highest MSWD at 1.8 and could be considered an errorchron since it has a degree of 1050 freedom of 9. This could explain why it is slightly older than the rest of the chondrule ages.

1051

1052 4.7 Chondrule formation mechanism

1053

1054 Several models have been proposed to explain the chondrule formation mechanism. The 1055 most common models are X-wind, gravity induced shock-wave, nebula lightning, bow shock 1056 around planetesimals and impact on planetesimals (Desch et al., 2012 and references therein). 1057 Among them, the gravity induced shock-wave inside a protoplanetary disk and the bow shock 1058 models best explain the cooling rates of chondrules of 10-1000 °C/h inferred from laboratory 1059 experiments (Connolly and Love, 1998; Desch and Connolly, 2002; Ciesla et al., 2004; Morris et 1060 al., 2012). Large-scale shock can either be produced by gravitational instability of massive disks 1061 or bow shocks from planetary embryos (Boss and Durisen, 2005; Morris et al., 2012; Hood and 1062 Weidenschilling, 2012). Another mechanism that has been proposed is the impact between 1063 planetary embryos that generated a vapor-melt plume for the formation of chondrules in CB 1064 chondrites (Krot et al., 2005). Such process has been modelled recently by several studies 1065 (Asphaug et al., 2011; Johnson et al., 2015). In this section we examine whether they are consistent 1066 with the constraint of a duration between 1.8 and 2.2 Ma after CAIs for OC chondrule formation 1067 and a main chondrule forming event at ~2 Ma.

1068 The X-wind model predicts that chondrule formation should concomitant to CAIs 1069 formation (Desch et al., 2012). This is clearly in contradiction with the results presented in this 1070 paper that show a delay of chondrule formation until ~1.8 Ma after CAIs. 1071 Large scale shock generated by gravitational instability inside a protoplanetary disk could 1072 have occurred very early during the disk accretion (≤1 Ma) and may be related to FU Orionis 1073 phenomenon (Boley and Durisen, 2008; Miller et al., 2011). Gravitational instability of the disk at 1074 a later stage could be produced by a spiral arm

generated by the growth of Jupiter. Boss and 1075 Durisen (2005) showed that gravitational instability beyond the Jupiter orbit produces inward 1076 spiral shock fronts at 2-3 AU that are capable of melting chondrules. Such shock-wave heating 1077 would successfully reproduce the thermal histories experimentally predicted from chondrule 1078 textures (Morris and Desch, 2010; Desch et al., 2012). The FeO-poor and FeO-rich chondrules are 1079 in this case only a function of the oxygen fugacity due to enrichment of oxygen compared to the 1080 canonical gas. Such instability could have been episodic, occurred in a short time (<1,000 yr), but 1081 repeated multiple times during the growth of Jupiter (Boss and Durisen, 2005), so that it may 1082 explain the total range of chondrules from 1.8 Ma to 2.2 Ma after CAIs. 1083 Another process to produce large scale shock in the disk could be bow shock created by 1084 planetary embryo or large (≥1000 km) planetesimals with eccentric orbits, which were excited by 1085 resonance with Jupiter (e.g., Ciesla et al., 2004; Morris et al., 2012: Hood and Weidenschilling 1086 2012). Morris et al. (2012) argued that Na-rich chondrules in UOCs might be successfully 1087 produced in the atmosphere of planetary embryo with high Na partial pressure, which derived from 1088 degassing of volatile by a magma ocean. A Mars size planetary embryo likely existed by 1.8 Ma 1089 (Dauphas and Pourmand, 2011), so that is consistent with the timing of UOC chondrule formation. 1090 The bow shock continues for a short period <0.1 Ma until the eccentric orbit of the planetary 1091 embryo is dampened, which is consistent with Na-rich chondrules with indistinguishable ages of $1092\ 2.03\ \pm\ 0.10\ Ma$ (Fig. 13b). The bow shock to produce chondrules could be repeated multiple times 1093 as the eccentric orbit would be excited again, which could easily explain the total duration of 0.4

1095 The impact between planetesimals to produce chondrules has been proposed (Asphaug et 1096 al., 2011; Sanders and Scott, 2012; Johnson et al., 2015) as an alternative mechanism to explain 1097 the high abundance of Na in chondrule olivine in UOCs (Alexander et al. 2008). Sanders and Scott 1098 (2012) showed the splashing model from impact between molten planetesimals where any chondrule formed before 1.5 Ma after CAIs could not survive the heat produce by the ²⁶ 1099 Al decay

1094 Ma.

inside a planetesimal. This is in good agreement with the fact that no ²⁶Al- 1100 ²⁶Mg ages older than 1101 1.7 Ma are found in chondrules. In the splashing model, chondrule production would stop at

~2.5 1102 Ma due to a thicker, cooler and mechanically stronger crust around planetesimals as their 1103 underlying magma oceans crystallized (Sanders and Scott, 2012). The lower limit for chondrule 1104 production would then represent the transition from a disk populated mainly by molten bodies of 1105 various sizes to a disk with fewer, larger bodies. However, the main problem for the molten 1106 planetesimal impact model is whether the interior of the planetesimal was fully molten without 1107 igneous differentiation to maintain chondritic bulk silicate compositions, as indicated by Wilson 1108 and Keil (2012).

1109 Johnson et al. (2015) modelled impact between planetesimal and planetary embryo that 1110

generates jetting to produce melted droplets. The model successfully reproduces the thermal 1111 history of chondrules, with cooling rates in the order of 10-1,000 K/h. They indicated that impact 1112 jetting could occur as early as 0.4 Ma after CAIs formation and continue as long as planetary 1113 embryos exist in the chondrule formation regions, which would have moved from inner disk to 1114 outer disk with time. Under this model, the lack of UOC chondrules older than 1.8 Ma would 1115 indicate the absence of planetary embryos in the ordinary chondrite formation region until ~1.8 Ma after CAIs. The ²⁶ 1116 Al ages of chondrules in carbonaceous chondrites are typically 2.2 Ma or 1117 younger (e.g., Nagashima et al., 2018 and references therein), which may be consistent with 1118 formation regions of carbonaceous chondrites to be farther out in the disk compared to ordinary 1119 chondrites.

1120 Chondrule formation events could be repeated multiple times until their parent asteroidal 1121 bodies formed for the shock-wave model. From our present dataset, accretion of L and LL 1122 chondrites could occur at ~2.15 Ma, which is consistent with the estimate a thermal model of the 1123 ordinary chondrites by Sugiura and Fujiya (2014) and Blackburn et al. (2017). Recently, several 1124 studies indicated an early formation of Jupiter <1 Ma after CAIs that separated inner and outer 1125 protoplanetary disk in order to explain the isotopic dichotomy between carbonaceous and non

1126 carbonaceous meteorites (Kruijer et al., 2017; Desch et al., 2018; Kruijer et al., 2020). If it was the 1127 case, many more chondrules could have been formed by large scale and/or bow shocks earlier than 1.8 Ma, they would not have survived the heat produced by ²⁶ 1128 Al decay if their parent bodies formed 1129 earlier than 1.5 Ma. Therefore, the observed range of Al-Mg ages from UOC chondrules may 1130

suggest either that a Jupiter formation that could produce large scale shock was delayed until 1.8 1131 Ma, or that UOC chondrules formed by the processes involving planetary embryos, such as bow 1132 shock and impact melting, and that the chondrules formed earlier than 1.5 Ma were totally melted due to the heat produced through the ²⁶ 1133 Al decay inside these planetesimals. The lower limit of 2.15 1134 Ma after CAIs found in this study would then mark the transition from a disk populated mainly by 1135 molten bodies of various sizes to a disk with fewer, larger bodies.

1136

1137

1138 **5. CONCLUSION**

1139

In this study we determined the inferred (26 Al/ 27 1140 Al) $_0$ of 17 porphyritic chondrules from 6 1141 different UOCs. These chondrules are mostly plagioclase-bearing chondrules with An₁₋₈₇ 1142 compositions and additional 3 glass-bearing chondrules were also studied. They show a wide range 1143 of chondrule types and compositions, for both their mafic minerals Mg# and mesostasis 1144 composition. Past improvement of the analytical configuration using a multi-collection of EM detectors allowed for the precise measurements of excess 1145 26 Mg in plagioclase and glass at the level 1146 of \pm 1.6-2% $_0$ from a single 4 μ m SIMS spot analyses for plagioclase and glass with ~0.1 wt.%

MgO content. This improved analytical capability allowed us to determine relative ²⁶Al- 1147 ²⁶Mg ages 1148 of chondrules with a precision typically at 0.1 Ma. We conclude the following: 1149 1) Plagioclase-bearing chondrules show the same textures and compositional variations than 1150 glass-bearing chondrules. The presence of plagioclase as the main mesostasis phase is 1151 likely the result of a slower cooling rate, either during the whole chondrule crystallization, 1152 or most probably at the very end. Plagioclase inside chondrules show clear evidence of 1153 crystallographic control on the incorporation of Mg and excess silica, with minimum 1154 contents at An₁₀₋₂₀ and An₂₀₋₄₀, for Mg and []Si₄O₈, respectively.

1155 2) Plagioclase-bearing chondrules have range of oxygen isotope ratios similar to those of 1156 glass-bearing chondrules. Plagioclase-bearing chondrules with higher An compositions (>50) have Δ^{17} O $\leq 0\%$, while those with lower An compositions show positive Δ^{17} 1157 O. 1158 There is no resolvable

difference between L and LL chondrites for host chondrule oxygen isotope signatures, including relationship between oxygen isotope ratios ($\delta^{18}O$ and Δ^{17} 1159 O) 1160 versus Mg# of mafic minerals.

3) All mesostases in 17 chondrules show resolvable δ 1161 ²⁶Mg*, except for small glass areas in 1162 two plagioclase-bearing chondrules. The 17 chondrules yield an isochron with MSWD between 0.34 and 1.8. Their inferred (²⁶Al/²⁷Al)₀ range from $(6.5 \pm 0.6) \times 10^{-6}$ 1163 to $(9.5 \pm 1.0) \times 10^{-6}$. Assuming a homogeneous distribution of ²⁶1164 Al in the Solar System with a canonical (²⁶Al/²⁷Al)₀ value of 5.25×10^{-5}

1165 at the time of CAI formation, these chondrules formed from $1.74 \pm {}^{0.12}$ 1166 /0.11 to 2.13 ± 0.09 Ma after CAIs. There is no resolvable difference 1167 between the ages of chondrules from L chondrites and LL chondrites. 1168 4) The duration for chondrule formation reported in this study of < 0.4 Ma is in very good 1169 agreement with recently published data from anorthite-bearing chondrule from Siron et al. 1170 (2021). However, this is in contradiction with longer duration estimated in studies by 1171 Villeneuve et al. (2009) and Pape et al. (2019). The youngest age observed from this study 1172 is consistent with the estimated time of accretion of ordinary chondrite parent bodies 1173 (Sugiura and Fujiya, 2014; Blackburn et al., 2017).

1174 5) A main chondrule forming event that produced most of the Na-rich chondrules occurred at 1175 \sim 2.0 Ma after CAIs. This event was likely very short, as highlighted by the albite-bearing chondrule (An < 30) ages that span a small range of ages between 1.99 \pm 0.10

1176 /0.09 Ma and 2.07 ± 0.11 1177 /0.10 Ma. Although they overlap within analytical uncertainties, Na-rich chondrule 1178 formation would have postdated the chondrule forming event responsible for anorthite 1179 bearing chondrules that could have been a separate event at ~1.9 Ma (Siron et al., 2021). 1180 6)

The timescale of UOC chondrule formation from this study was compared to existing 1181 models of chondrule formation. Onset of chondrule formation at 1.8 Ma may indicate the 1182 timing for the formation of Jupiter or planetary embryos that results in formation of 1183 chondrules in ordinary chondrite forming regions under large scale disk shock, bow shock 1184 and impact jetting models, or due to difficulty in preserving older chondrules in molten 1185 planetesimal

impact models. Ordinary chondrite chondrule formation had terminated by 1186 2.2 Ma by the subsequent accretion of L and LL chondrite parent bodies, as indicated from 1187 thermal models of ordinary chondrite parent bodies.

1188

1189

1190 ACKNOWLEDGMENTS

1191

(ANSMET) program which has been funded by NSF and NASA, and characterized and curated 1194 by the Department of Mineral Sciences of the Smithsonian Institution and Astromaterials Curation 1195 Office at NASA Johnson Space Center. We thank Steve Simon, University of New Mexico, 1196 Timothy McCoy, Smithsonian Institution, and ANSMET program for allocation of meteorite 1197 samples. We acknowledge extensive supports from John Fournelle for EPMA, Bil Schneider for 1198 SEM, and Michael Spicuzza and Peter Sobol for SIMS support. We thank the three anonymous 1199 reviewers and associate editor Anders Meibom for their constructive comments that helped 1200 improve the manuscript. This work is supported by NASA Emerging World Program 1201 (NNX17AE29G, N. K.). The upgrade of the RF plasma source is supported by the NASA 1202 Laboratory Analysis of Returned Samples and Planetary Major Equipment Programs 1203 (NNX16AG80G) and the NSF Instrumentation and Facility Program (EAR-1355590). WiscSIMS 1204 is partly supported by NSF (EAR-1658823). FIB instrumentation was supported by NSF through

1205 the University of Wisconsin Materials Research Science and Engineering Center (DMR 1206 17204015). This work was also supported by a Grant-in-aids of Ministry of Education, Science, 1207 Sport, and Culture of Japanese government, No. 18K03729 to M. K.

1208

1209 Appendix A. Supplementary Material

1210

1211 The following files can be downloaded as Supplementary Material: 1212 - Supplementary Material 1 is an excel file with all supplementary tables S1-12 1213 representing all geochemical data, i.e., oxygen

isotopes (Tables S1-4), Al-Mg isotopes 1214 (Tables S5-8) and major and minor elements from EPMA analyses (Tables S9-12). 1215 - Supplementary Material 2 is a text file that describes the EM gain used for EM-EM 1216 analyses of Al-Mg isotopes for mesostasis analyses (SM2-1) and the detailed 1217 petrographic description of all chondrules analyzed for oxygen and Al-Mg isotopes 1218 (SM2-2).

1219 - Supplementary Material 3 is a pdf file with BSE images of whole chondrules analyzed 1220 for oxygen and Al-Mg isotopes, high magnification images with the location of these 1221 analyses and very high magnification of the SIMS pits after the analyses.

1222

1223

1224 RESEARCH DATA

1225

1226 The raw data for the different SIMS sessions, the EDS spectrums and their locations, the 1227 BSE images for the whole chondrite sections can be found with this link:

1228 http://dx.doi.org/10.17632/xwpx2v5m4d.1 1229

1230

1231 REFERENCES

1232

- 1233 Agee C. B., Burkemper L. K., Muttik N. and Spilde M. N. (2013) New primitive prdinary 1234 chondrite: Northwest Africa 7731 (L3.00). 76th Annual Meteoritical Society Meeting, 1235 Edmonton, Canada. #5130(abstr.).
- 1236 Alexander C. M. O'D. and Ebel D. S. (2012) Questions, questions: Can the contradictions 1237 between the petrologic, isotopic, thermodynamic, and astrophysical constraints on chondrule 1238 formation be resolved? *Meteorit. Planet. Sci.* **47**, 1157–1175.
- 1239 Alexander C. M. O'D., Barber D. J. and Hutchison R. (1989) The microstructure of Semarkona 1240 and Bishunpur. *Geochim. Cosmochim. Acta* **53**, 3045–3057.
- 1241 Alexander C. M. O'D., Grossman J. N., Ebel D. S. and Ciesla F. J. (2008) The Formation 1242 Conditions of Chondrules and Chondrites. *Science* **320**, 1617–1619.
- 1243 Asphaug E., Jutzi M. and Movshovitz N. (2011) Chondrule formation during planetesimal 1244 accretion. *Earth Planet. Sci. Lett.* **308**, 369–379.
- 1245 Beaty D. W. and Albee A. L. (1980) Silica solid solution and zoning in natural plagioclase. 1246 *American Mineralogist* **65**, 63–74.
- 1247 Bischoff A. and Keil K. (1983) Ca-Al-rich chondrules and inclusions in ordinary chondrites.

- 1249 Blackburn T., Alexander C. M. O'D., Carlson R. and Elkins-Tanton L. T. (2017) The accretion 1250 and impact history of the ordinary chondrite parent bodies. *Geochim. Cosmochim. Acta* **200**, 1251 201–217.
- 1252 Boley A. C. and Durisen R. H. (2008) Gravitational instabilities, chondrule formation, and the 1253 FU Orionis phenomenon. *Astrophys. J.* **685**, 1193–1209.
- 1254 Bollard J., Kawasaki N., Sakamoto N., Olsen M., Itoh S., Larsen K., Wielandt D., Schiller M., 1255 Connelly J. N., Yurimoto H. and Bizzarro M. (2019) Combined U-corrected Pb-Pb dating 1256 and 26Al-26Mg systematics of individual chondrules Evidence for a reduced initial 1257 abundance of 26Al amongst inner Solar System chondrules. *Geochim. et Cosmochim. Acta* 1258 **260**, 62–83.
- 1259 Boss A. P. and Durisen R. H. (2005) Chondrule-forming Shock Fronts in the Solar Nebula: A 1260 Possible Unified Scenario for Planet and Chondrite Formation. *Astrophys. J.* **621**, L137–1261 L140.
- 1262 Brearley A. J. and Jones R. H. (1998) Chondritic meteorite. *In Planetary materials. Reviews in* 1263 *Mineralogy*, vol. 36. (ed. J. J. Papike). Mineralogical Society of America, Washington, D.C. 1264 pp. 3-1–3-398.
- 1265 Budde G., Kruijer T. S. and Kleine T. (2018) Hf-W chronology of CR chondrites: Implications for the timescales of chondrule formation and the distribution of ²⁶ 1266 Al in the solar nebula. 1267 *Geochim. Cosmochim. Acta* 222, 284–304.
- 1268 Catanzaro E. J., Murphy T. J., Garner E. L. and Shields W. R. (1966) Absolute isotopic 1269 abundance ratios and atomic weight of magnesium. *Journal of Research of the National* 1270 *Bureau of Standards* **70A**, 453–458.
- 1271 Ciesla F. J., Lauretta D. S. and Hood L. L. (2004) The frequency of compound chondrules and 1272 implications for chondrule formation. *Meteorit. Planet. Sci.* **39**, 531–544.
- 1273 Clayton R. N., Grossman L. and Mayeda T. K. (1973) A Component of Primitive Nuclear 1274 Composition in Carbonaceous Meteorites. *Science* **182**, 485.
- 1275 Clayton R. N., Onuma N., Grossman L. and Mayeda T. K. (1977) Distribution of the per-solar 1276 components in Allende and other carbonaceous chondrites. *Earth Planet. Sci. Lett.* **34**, 209–1277 224.
- 1278 Clayton R. N., Mayeda T. K., Goswami J. N. and Olsen E. J. (1991) Oxygen isotope studies of 1279 ordinary chondrites. *Geochim. Cosmochim. Acta* **55**, 2317–2337.
- 1280 Connolly H. C. Jr and Jones R. H. (2016) Chondrules: The canonical and noncanonical views. *J.* 1281 *Geophys. Res.*, 1–15.
- 1282 Connolly H. C. and Love S. G. (1998) The Formation of Chondrules: Petrologic Tests of the 1283 Shock Wave Model. *Science* **280**, 62–67.
- 1284 Cuzzi J. N., Hogan R. C. and Bottke W. F. (2010) Towards initial mass functions for asteroids 1285 and Kuiper Belt Objects. *Icarus* **208**, 518–538.
- 1286 Dauphas N. and Pourmand A. (2011) Hf–W–Th evidence for rapid growth of Mars and its status 1287 as a planetary embryo. *Nature* **473**, 489–492.
 - 1288 Davis A. M., Richter F. M., Mendybaev R. A., Janney P. E., Wadhwa M. and McKeegan K. D. (2015) Isotopic mass fractionation laws for magnesium and their effects on ²⁶Al– 1289 ²⁶Mg 1290

- 1291 Desch S. J. and Connolly H. C. Jr (2002) A model of the thermal processing of particles in solar 1292 nebula shocks: Application to the cooling rates of chondrules. *Meteorit. Planet. Sci.* **37**, 183–1293 207.
- 1294 Desch S. J., Morris M. A., Connolly H. C. Jr and Boss A. P. (2012) The importance of 1295 experiments: Constraints on chondrule formation models. *Meteorit. Planet. Sci.* 47, 1139–1296 1156. 1297 Desch S. J., Kalyaan A. and Alexander C. M. O'D. (2018) The Effect of Jupiter's Formation on 1298 the Distribution of Refractory Elements and Inclusions in Meteorites. *Astrophys. J. Suppl.* 1299 238, 11.
- 1300 Dohmen R. and Blundy J. (2014) A predictive thermodynamic model for element partitioning 1301 between plagioclase and melt as a function of pressure, temperature and composition. *Am. J.* 1302 *Sci.* **314**, 1319–1372.
- 1303 Donovan J. J., Singer J. W. and Armstrong J. T. (2016) A new EPMA method for fast trace 1304 element analysis in simple matrices. *Am. Mineral.* **101**, 1839–1853.
- 1305 Dunham E. T., Wadhwa M., Desch S. J. and Hervig R. L. (2020) Best Practices for Determination of Initial ¹⁰Be/⁹
- 1306 Be in Early Solar System Materials by Secondary Ion Mass 1307 Spectrometry. *Geostand. Geoanal. Res.* **52**, 1–16.
- 1308 Ebert S. and Bischoff A. (2016) Genetic relationship between Na-rich chondrules and Ca,Al-rich 1309 inclusions? Formation of Na-rich chondrules by melting of refractory and volatile precursors 1310 in the solar nebula. *Geochim. Cosmochim. Acta* 177, 182–204.
- 1311 Edwards G. H. and Blackburn T. (2020) Accretion of a large LL parent planetesimal from a 1312 recently formed chondrule population. *Sci. Adv.*, 1–9.
- 1313 Fukuda K., Beard B. L., Dunlap D. R., Spicuzza M. J., Fournelle J. H., Wadhwa M. and Kita N. 1314 T. (2020) Magnesium isotope analysis of olivine and pyroxene by SIMS: Evaluation of 1315 matrix effects. *Chem. Geol.* **540**, 119482.
- 1316 Fukuda K., Brownlee D. E., Joswiak D. J., Tenner T. J., Kimura M. and Kita N. T. (2021a) 1317 Correlated isotopic and chemical evidence for condensation origins of olivine in comet 1318 81P/Wild 2 and in AOAs from CV and CO chondrites. *Geochim. Cosmochim. Acta* **293**, 1319 544–574.
- 1320 Fukuda K., Hiyagon H., Fujiya W., Kagoshima T., Itano K., Iizuka T., Kita N. T. and Sano Y. (2021b) Irradiation origin of ¹⁰ 1321 Be in the solar nebula: Evidence from Li-Be-B and Al-Mg 1322 isotope systematics, and REE abundances of CAIs from Yamato-81020 CO3.05 chondrite. 1323 *Geochim. Cosmochim. Acta* **293**, 187–204.
- 1324 Grossman J. N. (1988) Chondrites and the solar nebula. *Nature* **334**, 14–15.
- 1325 Grossman J. N. and Brearley A. J. (2005) The onset of metamorphism in ordinary and 1326 carbonaceous chondrites. *Meteorit. Planet. Sci.* **40**, 87–122.
- 1327 Grossman J. N., Alexander C. M. O'D., Wang J. and Brearley A. J. (2000) Bleached chondrules: 1328 Evidence for widespread aqueous processes on the parent asteroids of ordinary chondrites. 1329 *Meteorit. Planet. Sci.* **35**, 467–486.
- 1330 Grossman J. N., Alexander C. M. O'D., Wang J. and Brearley A. J. (2002) Zoned chondrules in 1331 Semarkona: Evidence for high- and low-temperature processing. *Meteorit. Planet. Sci.* **37**, 1332

- 49–73.

 1333 Guo C. and Zhang Y. (2016) Multicomponent diffusion in silicate melts: SiO –TiO –Al O 2 2 3 3
- 1334 MgO–CaO–Na O–K 2O System. *Geochim. Cosmochim. Acta* **195**, 126–141.
- Hertwig A. T., Kimura M., Ushikubo T., Defouilloy C. and Kita N. T. (2019) The ²⁶Al–1335 ²⁶Mg 1336 systematics of FeO-rich chondrules from Acfer 094: Two chondrule generations distinct in 1337 age and oxygen isotope ratios. Geochim. Cosmochim. Acta 253, 111–126.
- 1338 Hood L. L. and Weidenschilling S. J. (2012) The planetesimal bow shock model for chondrule 1339 formation: A more quantitative assessment of the standard (fixed Jupiter) case. *Meteorit*. 1340 Planet. Sci. 47, 1715–1727.
- 1341 Hutcheon I. D. and Hutchison R. (1989) Evidence from the Semarkona ordinary chondrite for ²⁶ 1342 Al heating of small planets. *Nature* **337**, 238–241.
- Hutcheon I. D. and Jones R. H. (1995) The ²⁶Al- 1343 ²⁶Mg record of chondrules: clues to nebular 1344 chronolgy. Lunar and Planetary Sciences 25, 587–588.
- 1345 Ikeda Y. (1983) Major element chemical compositions and chemical types of chondrules in 1346 unequilibrated E, O, and C chondrites from Antarctica. Mem. NIPR Spec. Iss., 30 (1983), 1347 pp. 122–145.
- 1348 Jacobsen B., Yin Q.-Z., Moynier F., Amelin Y., Krot A. N., Nagashima K., Hutcheon I. D. and Palme H. (2008) ²⁶Al-²⁶Mg and ²⁰⁷Pb-²⁰⁶ 1349 Pb systematics of Allende CAIs: Canonical solar initial ²⁶Al/²⁷ 1350 Al ratio reinstated. *Earth Planet. Sci. Lett.* **272**, 353–364.
- 1351 Johnson B. C., Minton D. A., Melosh H. J. and Zuber M. T. (2015) Impact jetting as the origin of 1352 chondrules. Nature 517, 339-341.
- 1353 Jones R. H. (1994) Petrology of FeO-poor, porphyritic pyroxene chondrules in the Semarkona 1354 chondrite. Geochim. Cosmochim. Acta 58, 5325–5340.
- 1355 Jones R. H. (2012) Petrographic constraints on the diversity of chondrule reservoirs in the 1356 protoplanetary disk. Meteorit. Planet. Sci. 47, 1176–1190.
- 1357 Jones R. H. and Lofgren G. E. (1993) A comparison of FeO-rich, porphyritic olivine chondrules 1358 in unequilibrated chondrites and experimental analogues. *Meteoritics* **28**, 213–221.
- 1359 Kimura M., Grossman J. N. and Weisberg M. K. (2008) Fe-Ni metal in primitive chondrites: 1360 Indicators of classification and metamorphic conditions for ordinary and CO chondrites. 1361 Meteorit. Planet. Sci. 43, 1161–1177.
- Kita N. T. and Ushikubo T. (2012) Evolution of protoplanetary disk inferred from ²⁶ 1362 Al 1363 chronology of individual chondrules. *Meteorit. Planet. Sci.* 47, 1108–1119.
- 1364 Kita N. T., Nagahara H., Togashi S. and Morishita Y. (2000) A short duration of chondrule formation in the solar nebula: Evidence from ²⁶ 1365 Al in Semarkona ferromagnsian chondrules. 1366 Geochim. Cosmochim. Acta 64, 3913–3922.
- 1367 Kita N. T., Nagahara H., Tachibana S., Tomomura S., Spicuzza M. J., Fournelle J. H. and Valley 1368 J. W. (2010) High precision SIMS oxygen three isotope study of chondrules in LL3 1369 chondrites: Role of ambient gas during chondrule formation. Geochim. Cosmochim. Acta 74, 1370 6610-6635.
- 1371 Kita N. T., Ushikubo T., Knight K. B., Mendybaev R. A., Davis A. M., Richter F. M. and

- Fournelle J. H. (2012) Internal ²⁶Al– 1372 ²⁶Mg isotope systematics of a Type B CAI: Remelting 1373 of refractory precursor solids. *Geochim. Cosmochim. Acta* **86**, 37–51.
- 1374 Kita N. T., Yin Q.-Z., MacPherson G. J., Ushikubo T., Jacobsen B., Nagashima K., Kurahashi E., Krot A. N. and Jacobsen S. B. (2013) ²⁶Al– 1375 ²⁶Mg isotope systematics of the first solids in 1376 the early solar system. *Meteorit. Planet. Sci.* **48**, 1383–1400.
- 1377 Krot A. N., Amelin Y., Cassen P. and Meibom A. (2005) Young chondrules in CB chondrites 1378 from a giant impact in the early Solar System. *Nature* **436**, 989–992.
- 1379 Kruijer T. S., Kleine T., Borg L. E., Brennecka G. A., Irving A. J., Bischoff A. and Agee C. B. 1380 (2017) The early differentiation of Mars inferred from Hf–W chronometry. *Earth Planet*. 1381 *Sci. Lett.* **474**, 345–354.
- 1382 Kruijer T. S., Kleine T. and Borg L. E. (2020) The great isotopic dichotomy of the early Solar 1383 System. *Nature Astronomy* **4**, 32–40.
- Kurahashi E., Kita N. T., Nagahara H. and Morishita Y. (2008) ²⁶Al– 1384 ²⁶Mg systematics of 1385 chondrules in a primitive CO chondrite. *Geochim. Cosmochim. Acta* **72**, 3865–3882.
- 1386 Larsen K. K., Trinquier A., Paton C., Schiller M., Wielandt D., Ivanova M. A., Connelly J. N., 1387 Nordlund Å., Krot A. N. and Bizzarro M. (2011) Evidence for magnesium isotope 1388 heterogeneity in the solar protoplanetary. *Astrophys. J.* **735**, L37–7.
- 1389 Lewis J. A. and Jones R. H. (2019) Primary feldspar in the Semarkona LL3.00 chondrite: 1390 Constraints on chondrule formation and secondary alteration. *Meteorit. Planet. Sci.* **54**, 72–1391 89.
- 1392 Lewis J. A., Jones R. H. and Brearley A. J. (2022) Plagioclase alteration and equilibration in 1393 ordinary chondrites: Metasomatism during thermal metamorphism. *Geochim. Cosmochim.* 1394 *Acta* **316**, 201–229.
- 1395 Libourel G. and Chaussidon M. (2011) Oxygen isotopic constraints on the origin of Mg-rich 1396 olivines from chondritic meteorites. *Earth Planet. Sci. Lett.* **301**, 9–21.
- 1397 Lofgren G. E. (1989) Dynamic crystallisation of chondrule melts of porphyritic olivine 1398 composition: Textures experimental and natural. *Geochim. Cosmochim. Acta* **53**, 461–470.
- 1399 Miller A. A., Hillenbrand L. A., Covey K. R., Poznanski D., Silverman J. M., Kleiser I. K. W., 1400 Rojas-Ayala B., Muirhead P. S., Cenko S. B., Bloom J. S., Kasliwal M. M., Filippenko A. 1401 V., Law N. M., Ofek E. O., Dekany R. G., Rahmer G., Hale D., Smith R., Quimby R. M., 1402 Nugent P., Jacobsen J., Zolkower J., Velur V., Walters R., Henning J., Bui K., McKenna D., 1403 Kulkarni S. R., Klein C. R., Kandrashoff M. and Morton A. (2011) Evidence for an FU 1404 Orionis-like outburst from a T Tauri star. *Astrophys. J.* 730, 80–14.
- 1405 Morris M. A. and Desch S. J. (2010) Thermal histories of chondrules in solar nebula shocks. 1406 *Astrophys. J.* **722**, 1474–1494.
- 1407 Morris M. A., Boley A. C., Desch S. J. and Athanassiadou T. (2012) Chondrule formation in 1408 bow shocks around eccentric planetary. *Astrophys. J.* **752**, 27–17.
- 1409 Nagahara H., Kita N. T., Ozawa K. and Morishita Y. (2008) Condensation of major elements 1410 during chondrule formation and its implication to the origin of chondrules. *Geochim.* 1411 *Cosmochim. Acta* **72**, 1442–1465.
 - Nagashima K., Kita N. T. and Luu T.-H. (2018) ²⁶Al– 1412 ²⁶Mg systematics of chondrules. In

- 1413 *Chondrules: Records of Protoplanetary Disk Processes* (eds. S. S. Russell, H. Connolly and 1414 A. N. Krot). Cambridge University Press, Cambridge U.K., pp. 247–275.
- Nishiizumi K. (2004) Preparation of ²⁶ 1415 Al AMS standards. *Nuclear Instruments and Methods in* 1416 *Physics Research Section B: Beam Interactions with Materials and Atoms* **223-224**, 388–1417 392.
- 1418 Pape J., Mezger K., Bouvier A. S. and Baumgartner L. P. (2019) Time and Duration of Chondrule Formation: Constraints from ²⁶Al– 1419 ²⁶Mg Ages of Individual Chondrules. 1420 *Geochim. Cosmochim. Acta* **244**, 416–436.
- 1421 Pape J., Rosén Å. V., Mezger K. and Guillong M. (2021) Primary crystallization and partial 1422 remelting of chondrules in the protoplanetary disk: Petrographic, mineralogical and chemical 1423 constraints recorded in zoned type I chondrules. *Geochim. Cosmochim. Acta* **292**, 499–517.
- 1424 Rocha S. E. and Jones R. H. (2012) An experimental study of the conditions of type II chondrule 1425 formation in ordinary chondrites. 43*rd Lunar Planet. Sci. XXXXIII*. Lunar Planet. Inst., 1426 Houston. #2595 (abstr.).
- 1427 Ruzicka A., Grossman J., Bouvier A. and Agee C. B. (2017) The Meteoritical Bulletin, No. 103. 1428 *Meteorit. Planet. Sci.* **52**, 1014–1014.
- 1429 Sanders I. S. and Scott E. R. D. (2012) The origin of chondrules and chondrites: Debris from 1430 low-velocity impacts between molten planetesimals? *Meteorit. Planet. Sci.* **47**, 2170–2192.
- Siron G., Fukuda K., Kimura M. and Kita N. T. (2021) New constraints from ²⁶Al– 1431 ²⁶Mg 1432 chronology of anorthite-bearing chondrules in unequilibrated ordinary chondrites. *Geochim.* 1433 *Cosmochim. Acta* **293**, 103–126.
- Sugiura N. and Fujiya W. (2014) Correlated accretion ages and ε^{54} 1434 Cr of meteorite parent bodies 1435 and the evolution of the solar nebula. *Meteorit. Planet. Sci.* **49**, 772–787. 1436 Tenner T. J., Ushikubo T., Kurahashi E., Kita N. T. and Nagahara H. (2013) Oxygen isotope 1437 systematics of chondrule phenocrysts from the CO3.0 chondrite Yamato 81020: Evidence 1438 for two distinct oxygen isotope reservoirs. *Geochim. Cosmochim. Acta* **102**, 226–245.
- 1439 Tenner T. J., Nakashima D., Ushikubo T., Kita N. T. and Weisberg M. K. (2015) Oxygen isotope 1440 ratios of FeO-poor chondrules in CR3 chondrites: Influence of dust enrichment and H₂O 1441 during chondrule formation. *Geochim. Cosmochim. Acta* **148**, 228–250.
- 1442 Tenner T. J., Nakashima D., Ushikubo T., Tomioka N., Kimura M., Weisberg M. K. and Kita N. 1443 T. (2019) Extended chondrule formation intervals in distinct physicochemical environments: 1444 Evidence from Al-Mg isotope systematics of CR chondrite chondrules with unaltered 1445 plagioclase. *Geochim. Cosmochim. Acta* **260**, 133–160.
- 1446 Tronche E. J., Hewins R. H. and MacPherson G. J. (2007) Formation conditions of aluminum 1447 rich chondrules. *Geochim. Cosmochim. Acta* **71**, 3361–3381.
- 1448 Ushikubo T., Kimura M., Kita N. T. and Valley J. W. (2012) Primordial oxygen isotope 1449 reservoirs of the solar nebula recorded in chondrules in Acfer 094 carbonaceous chondrite. 1450 *Geochim. Cosmochim. Acta* **90**, 242–264.
- 1451 Ushikubo T., Nakashima D., Kimura M., Tenner T. J. and Kita N. T. (2013) Contemporaneous 1452 formation of chondrules in distinct oxygen isotope reservoirs. *Geochim. et Cosmochim. Acta* 1453 **109**, 280–295.
- Ushikubo T., Tenner T. J., Hiyagon H. and Kita N. T. (2017) A long duration of the \$^{16}\$ 1454 O-rich 1455

reservoir in the solar nebula, as recorded in fine-grained refractory inclusions from the least 1456 metamorphosed carbonaceous chondrites. Geochim. et Cosmochim. Acta 201, 103–122.

1457 Van Orman J. A., Cherniak D. J. and Kita N. T. (2014) Magnesium diffusion in plagioclase: Dependence on composition, and implications for thermal resetting of the ²⁶Al- 1458 ²⁶Mg early 1459 solar system chronometer. Earth Planet. Sci. Lett. 385, 79–88.

1460 Vermeesch P. (2012) On the visualisation of detrital age distributions. Chem. Geol. 312-313, 1461 190–194.

1462 Vermeesch P. (2018) IsoplotR: A free and open toolbox for geochronology. Geosci. Front. 9, 1463 1479-1493.

Villeneuve J., Chaussidon M. and Libourel G. (2009) Homogeneous Distribution of ²⁶ 1464 Al in the 1465 Solar System from the Mg Isotopic Composition of Chondrules. Science 325, 985–988.

1466 Wendt I. and Carl C. (1991) The statistical distribution of the mean squared weighted deviation. 1467 Chem. Geol. **86**, 275–285.

1468 Wick M. J. and Jones R. H. (2012) Formation conditions of plagioclase-bearing type I 1469 chondrules in CO chondrites: A study of natural samples and experimental analogs. 1470 Geochim. Cosmochim. Acta 98, 140–159.

1471 Wilson L. and Keil K. (2012) Volcanic activity on differentiated asteroids: A review and 1472 analysis. *Geochemistry* **72**, 289–321.

York D., Evensen N. M., Marti 1473 nez M. L. and De Basabe Delgado J. (2004) Unified equations for 1474 the slope, intercept, and standard errors of the best straight line. American Journal of Physics 1475 **72**, 367–375.

1476

1477 FIGURE CAPTIONS

1478

1479 Fig. 1. BSE images of plagioclase-bearing chondrules examined in this study. (a) NWA 8649 c62 1480 (type I PP), (b) QUE 97008 c12 (type I PP), (c) QUE 97008 c41 (type I PP), (d) QUE 97008 c68 1481 (type I PP), (e) NWA 8649 c27 (type I PP), (f) QUE 97008 c134 (type II PP), (g) NWA 8649 c12 1482 (type II PP), h) NWA 7731 c33 (type II POP). Abbreviations are as follow: olivine (Ol), pyroxene 1483 (Px), plagioclase (Pl). Scale bar is 250 µm. See text for a more detailed description of the different 1484 phases and compositions.

1485

1486

1487 Fig. 2. BSE images of chondrules examined in this study. (a-f) plagioclase-bearing chondrules and 1488 (g-h) glass-bearing chondrules. (a) NWA 8276 c22 (type II POP), (b) NWA 8276 c43 (type II 1489 POP), (c) QUE 97008 c102 (type II POP, (d) QUE 97008 c140 (type II POP), (e) Semarkona c55 1490 (type II POP), (f) MET 00452 c85 (type II PO), (g) QUE 97008 c31 (type II PP), (h) NWA 8649 1491 c116 (type II PP). Abbreviations are same as those in Fig. 1 and Gl for glass. Scale bar is 250 µm. 1492 See text for a more detailed description of the different phases and compositions. 1493

1494

1495 Fig. 3. BSE images of chondrules examined in this study. (a) MET 00452 c85 (type II PO). (b-e) 1496 Detailed textures of chondrule mesostasis; (b) MET 00452 c85, (c) MET 00526 c65 (glass-bearing 1497 type II PO), (d) plagioclase in Semarkona c55, (e) NWA 7731 c52 (glass-bearing type II POP). (f) 1498 close-up image of NWA 8276 c43 showing weathering vein with small fractures filled with a Fe 1499 rich phase (black arrows). The black and white square in the middle of the image represents the 1500 platinum deposition (3 µm white square) and small FIB mark (dark 1 µm square in the middle) 1501 that were used to locate SIMS analyses. (g) Enlarged image of a mesostasis area of QUE 97008 1502 c31 (glass-bearing type II PP) showing metal blob corona alteration in the lower right corner of 1503 the image. (h) Enlarged image of mesostasis glass in QUE 97008 c68. Mineral abbreviations are 1504 same as those in Figs. 1-2. Scale bar is 250 μ m for (a), 25 μ m for (b-g) and (h), and 10 μ m for (f).

1505 See text for a more detailed description of the different phases and compositions.

1506

1507

1508

1509 Fig. 4. Composition of plagioclase and glass in chondrule mesostasis. (a) Anorthite content, An = 1510 Ca / (Ca + Na +K) mole%, of plagioclase versus average Mg# of olivine or pyroxene in individual 1511 chondrules. Data from this study (circles) include EPMA analyses of plagioclase from 51 1512 chondrule where Mg# are taken from SEM-EDS analyses. Larger circles represent the plagioclases 1513 from chondrules analyzed for their Al-Mg isotopes. Diamonds refers to anorthite-bearing 1514 chondrule analyzed by Siron et al. (2021; S21). (b) MgO (wt.%) content and (c) excess silica

1515 ([]Si₄O₈) versus An in plagioclase from the same set of data in (a). Symbols are same as those in 1516 (a). (d) K₂O content (wt.%) of plagioclase (orange circles) and glass (blue diamonds) versus 1517 average Mg# of olivine or pyroxene in individual chondrules. Plagioclase analyses are from this 1518 study and Siron et al. (2021) while glass analyses are from this study only. The dashed line 1519 represents the detection limit (D.L.) of EPMA analyses for K₂O.

1520

1521

1522 Fig. 5. Individual oxygen three-isotope analyses in chondrules: (a) QUE 97008 c41, (b) NWA 1523 7731 c31, (c) NWA 7731 c34, (d) NWA 7731 c73, (e) NWA 8649 c12, (f) NWA 8276 c43, (g) 1524 NWA 8276 c59, (h) Semarkona c55, (i) MET 00452 c85. Symbols of minerals and reference lines 1525 are as follow, circles: olivine, diamonds: pyroxene, TFL: Terrestrial Fractionation Line (Clayton 1526 et al., 1973), ECL: Equilibrated Chondrite Line (Clayton et al., 1991), PCM: Primitive Chondrule 1527 Minerals line (Ushikubo et al., 2012), CCAM: Carbonaceous Chondrite Anhydrous Mineral line 1528 (Clayton et al., 1977). Error bars represent 2SD of bracketing standards. Light symbols are data 1529 excluded from the host chondrule computation.

1530

1531 Fig. 6. Individual oxygen three-isotope analyses in chondrules: (a) NWA 8649 c27, (b) NWA 8649 1532 c116, (c) NWA 7731 c14, (d) NWA 7731 c49, (e) NWA 7731 c52, (f) QUE 97008 c102, (g) NWA 1533 7731 c33, (h) NWA 8276 c22, (i) NWA 8649 c62. Reference lines and symbols are the same as 1534 those in Fig. 5.

1535

1536

1537 Fig. 7. . Individual oxygen three-isotope analyses in chondrules: (a) QUE 97008 c31, (b) QUE 1538 97008 c140, (c) NWA 7731 c5, (d) NWA 7731 c17, (e) NWA 7731 c24, (f) NWA 7731 c28, (g) 1539 QUE 97008 c12, (h) QUE 97008 c68, (i) QUE 97008 c134. Reference lines and symbols are the 1540 same as those in Fig. 5.

1541

Fig. 8. Host chondrule δ^{18} O vs δ^{17} 1542 O plot for porphyritic chondrules in UOCs (3.00-3.05) from this 1543 study. (a) type I porphyritic chondrules, (b) type II porphyritic chondrules, and (c) chondrules 1544 analyzed for Al-Mg chronology in this study. Literature data for porphyritic chondrules (K10; Kita 1545 et al., 2010) and anorthite-bearing chondrules (S21; Siron et al., 2021) are shown as comparison. 1546 Error bars are displayed for data from this study that represent propagated 2SE. 1547

1548 Fig. 9. Host chondrule oxygen isotope ratios vs Mg# of olivine/pyroxene of all chondrules studied here for oxygen isotopes. (a) δ^{18} O vs Mg# and (b) Δ^{17} 1549 O values vs Mg#. Chondrules that were 1550 analyzed for Al-Mg chronology are shown separately according to their mesostasis compositions 1551 and those analyzed only for oxygen isotopes are shown as open circles. Literature data of 1552 porphyritic chondrules (K10; Kita et al., 2010) are shown as crosses and those of anorthite-bearing 1553 chondrules (S21; Siron et al., 2021) are shown as squares. Error bars for chondrules from this study represent propagated 2SE for δ^{18} O and Δ^{17} 1554 O and 1SD of the 8 points used for oxygen analyses for

1555 Mg#.

1556

1557 Fig. 10. Internal isochron regression for 9 chondrules studied here. Diamonds represent olivine and pyroxene at the origin and plagioclases at high ²⁷Al/ 1558 ²⁴Mg, circles represent glass analyses. 1559 Error bars represent 2SE. The solid lines represent the regressions and dash lines are 95% confidence interval on the fit. Uncertainties for (²⁶Al/²⁷Al)₀ and (δ 1560 ²⁶Mg*)₀ are 2SE. Insets for f) 1561 and h) show expanded view of glass analyses for QUE 97008 c140 and NWA 8276 c43, 1562 respectively, which are off the isochron regressions lines from plagioclase analyses. 1563 1564

1565 Fig. 11. Internal isochron regression for 8 chondrules studied here. Symbols and lines are the same 1566 as in Fig. 10.

1567

1568

1569 Fig. 12. BSE images of plagioclase Al-Mg isotope analysis spots close to each other that show variations in their 27 Al/ 24 Mg and excess 1570 26 Mg outside their respective uncertainties. Scale bars are 1571 10 µm. (a) Two plagioclase analyses in QUE 97008 c140 at less than 10 µm from each other, b) 1572 Three plagioclase analyses in NWA 8649 c12 several to 10 µm from each other. Especially the two analyses on the lower side of the image show both 27 Al/ 24 Mg and δ 1573 26 Mg* varying by a factor 1574 of two. Bright areas near SIMS pits are platinum deposition that was applied for accurate targeting 1575 of SIMS primary beam positions (see section 2.2)

15761577

Fig. 13. Compilation of initial 26 Al/ 27 1578 Al ratios (upper axis) and corresponding ages after CAIs 1579 (lower axis) computed from internal isochron for each chondrule from this study. Data are sorted 1580 by meteorites in (a) and An contents of plagioclase and glass in (b). Chondrule type as follow: type 1581 I (open symbols) and type II (black filled symbols). Grey filled circle symbols represent anorthite 1582 bearing chondrules from UOCs studied by Siron et al. (2021), labelled as S21. Plagioclase and 1583 glass An content is computed as An = CaO / (CaO + Na₂O + K₂O) in mole%. Errors are 2SE for (26 Al/ 27 1584 Al)o ratios and 1SD for An content. The color-coded map in (b) represents the 2D kernel 1585 density estimate for plagioclase-bearing chondrules from this study and Siron et al. (2021). 1586 1587

1588 Fig. 14. Kernel density function for the distribution of Al-Mg ages of UOC chondrules. (a) Kernel 1589 density function for the distribution of chondrule Al-Mg ages are compared among plagioclase 1590 (red) and glass-bearing (green) chondrules from this study and anorthite-bearing (blue) chondrules 1591 from Siron et al. (2021; labelled as S21). (b) Kernel density function for UOC chondrule ages after 1592 CAIs are compared between data using small spots (blue; this study; Kita et al., 2000; Bollard et 1593 al., 2019; Siron et al., 2021) and using large spots (red; Villeneuve et al., 2009; Pape et al., 2019). 1594 Ages after CAIs from Kita et al. (2000), Villeneuve et al. (2009), Bollard et al. (2019) and Pape et al. (2019) were recalculated from their inferred (²⁶Al/²⁷ 1595 Al)₀ by applying a canonical value of 5.25×10⁻⁵ for CAIs and ²⁶Al half-life of 7.05×10⁵

1596 y 1597

Fig. 15. The inferred (26 Al/ 27 Al)₀ versus maximum 27 Al/ 1598 24 Mg for each chondrule. Data are shown 1599 from this study, Kita et al. (2000), Villeneuve et al. (2009), Bollard et al. (2000), Pape et al. (2019) 1600 and Siron et al. (2021). The transparency represents the P-value for their MSWD, the lower the P 1601 value, the more transparent the symbol. 1602

1603

Table 1: List of meteorites and numbers of chondrules examined in this study

Meteorite Classification Weathering Section EPMA O isotope Al-Mg Semarkona LL3.00 fall USNM 1805-9 (PTS) 14 1 1 Smithsonian National Museum of Natural History NWA 7731 L3.00 PTS^b 18 11 1 University of New Mexico NWA 8276 L3.00 W1 PM^b 10 3 3 University of New Mexico NWA 8649 LL3.05 W3 AZ-1-1^b, AZ-1-2^b(PM) 14 4 4 University of New Mexico QUE 97008 L3.05 A PTS #12, #14^b 23 7 7 US Antarctic meteorite program MET 00452^c L/LL 3.05

B/Ce PTS #16, #18^b 2 1 1 US Antarctic meteorite program MET 00526^c L/LL 3.05 B/C PTS #34^b, #54^b 8 US Antarctic meteorite program LEW 86134 L3.0 B/C PTS #17^b, #18^b US Antarctic meteorite program Total numbers of chondrules 89 27 17

^a Section names and numbers are shown when available. PTS- polished thin section, PM- polished mount. ^b Sections used for Fe-Ni metal observation. ^c Paired meteorites.

Table 2. Average major and minor elements for olivine composition determined with EPMA.

QUE 97008, 12 NWA 7731 NWA 8276 MET 00452, 16 Semarkona NWA 8649, <u>AZ-1-1</u> c12 c41 c68 c102 c134 <u>LPx</u> c134 <u>HPx</u> c140 Lpx c140 meso c33 min c33 min c23 min c43 max c52 c45 min c45 max c55 c85 min c55 LPx c55

 $SiO_2 40.88\ 40.65\ 41.34\ 38.39\ 39.17\ 37.61\ 39.24\ 38.41\ 38.09\ 39.74\ 39.05\ 38.50\ 40.30\ 39.79\ 37.67\ 40.52\ 39.14\ 38.29\ 39.37\ TiO_2\ 0.02\ 0.02\ 0.02\ 0.02\ 0.02\ 0.02\ 0.01\ 0.03\ b.d.l.\ b.$

 $\begin{array}{c} \text{Si } 0.994 \ 0.986 \ 0.992 \ 0.983 \ 0.982 \ 0.994 \ 0.987 \ 0.987 \ 0.991 \ 0.988 \ 0.993 \ 1.001 \ 0.995 \ 0.991 \ 0.985 \ 0.986 \ 0.992 \ 0.991 \ 0.993 \ \text{Al } 0.001 \$

 $\begin{array}{c} Mg\ 1.832\ 1.852\ 1.909\ 1.631\ 1.743\ 1.465\ 1.717\ 1.606\ 1.548\ 1.746\ 1.652\ 1.533\ 1.794\ 1.736\ 1.510\ 1.807\ 1.680\ 1.572\ 1.666\ Fe\ 0.156\ 0.160\ 0.089\ 0.379\ 0.274\ 0.495\ 0.287\ 0.388 \\ 0.432\ 0.254\ 0.342\ 0.426\ 0.205\ 0.265\ 0.490\ 0.206\ 0.302\ 0.402\ 0.329\ Ca\ 0.005\ 0.002\ 0.002\ 0.005\ 0.003\ 0.006\ 0.003\ 0.005\ 0.004\ 0.002\ 0.003\ 0.005\ 0.001\ 0.002\ 0.003\ 0.005\ 0.001\ 0.002\ 0.003\ 0.005\ 0.001\ 0.$

Fo 9 2 92 96 81 86 75 86 81 78 87 83 78 90 87 76 90 85 80 84 $^{\circ}$ Fo = Mg / (Mg + Fe) mole%. "Lpx" and "Hpx" indicate olivine chadacrysts in low-Ca pyroxene and high-Ca pyroxene and "meso" indicate olivine in chondrule mesostasis. Olivine compositions with highest and least Fo in chondrules are shown as "min" and "max" for NWA 8276 c43 and MET 00426 c85. b.d.l. below detection limit

Table 3. Average major and minor elements for pyroxene composition determined with EPMA

OUE 97008. 12 NWA 7731 NWA 8276 Semarkona NWA 8649. AZ-1-1 c12 c31 c41 c68 c102 c134 c140 c33 c22 c43 c59 c55 c12 c27 c62 c116 SiO₂ 57.75 55.81 57.19 57.85 55.13 56.03 55.85 55.43 55.45 56.15 55.21 56.14 55.57 56.96 58.16 55.70 TiO_2 0.05 0.01 0.03 0.05 0.05 0.03 0.04 0.05 0.03 0.02 0.06 0.04 0.03 0.11 0.10 0.01 Al_2O_3 0.36 0.15 0.27 0.44 0.43 0.19 0.36 0.22 0.32 0.26 0.57 0.27 0.34 1.07 0.65 0.19 MgO 36.44 30.94 35.00 37.34 31.94 33.82 32.69 30.75 29.94 31.65 29.40 32.60 31.52 34.92 38.38 30.38 FeO 4.12 11.34 6.37 3.07 9.63 8.44 8.89 10.86 12.20 10.00 11.91 8.57 10.89 5.10 1.76 12.86 CaO 0.24 0.19 0.20 0.26 0.73 0.16 0.48 0.58 0.64 0.28 0.34 0.39 0.26 0.41 0.37 0.22 Na_2O b.d.l. b.

 $\begin{array}{c} \text{Si } 1.981 \ 1.989 \ 1.98 \ 1.975 \ 1.97 \ 1.970 \ 1.973 \ 1.974 \ 1.98 \ 1.990 \ 1.989 \ 1.979 \ 1.971 \ 1.972 \ 1.97 \ 1.98 \ \text{Ti } 0.001 \ 0.000 \ 0.001 \ 0.000 \ 0.001 \ 0.000 \ 0.001 \ 0.000 \ 0.001 \ 0.000 \ 0.001$

 $\begin{array}{c} Mg~1.863~1.643~1.81~1.900~1.70~1.773~1.722~1.633~1.60~1.672~1.579~1.713~1.67~1.801~1.94~1.61~Fe~0.118~0.338~0.18~0.088~0.29~0.248~0.263\\ 0.324~0.37~0.297~0.359~0.253~0.32~0.148~0.05~0.38~Ca~0.009~0.007~0.01~0.009~0.03~0.006~0.018~0.022~0.02~0.011~0.013~0.015~0.01~0.015~0.01\\ 0.01~Mn~0.013~0.013~0.01~0.013~0.01~0.010~0.014~0.015~0.01~0.015~0.019~0.012~0.01~0.009~0.01~0.01~Cr~0.016~0.019~0.02~0.017~0.02~0.013~0.02~0.019~0.024~0.010~0.02~0.022~0.01~0.02~0.000~0.000~0.000~0.000~0.001~0.002~0.002~0.000~0.000~0.000~0.001~0.002\\ 0.00~Sum~Oct~2.022~2.021~2.03~2.027~2.05~2.054~2.038~2.009~2.02~2.013~1.994~2.003~2.04~1.995~2.02~2.03\\ \end{array}$

Table 4. Average major and minor elements for plagioclase composition determined with EPMA.

QUE 97008, 12 NWA 7731 NWA 8276 MET 00452, 16 Semarkona NWA 8649, AZ-1-1

1.74 Sum 3.98 3.98 3.97 3.97 3.95 3.98 3.96 3.97 3.97 3.96 3.98 3.96 3.97 3.92

c12 c41 c68 c102 c134 c140 c33 c22 c43 c85 c55 c12 c27 c27

c62 core

 $SiO_2 58.40 \, 57.83 \, 56.11 \, 52.81 \, 56.40 \, 64.32 \, 68.33 \, 65.56 \, 68.26 \, 68.23 \, 59.32 \, 65.85 \, 50.47 \, 54.11 \, 47.05 \, \text{TiO}_2 \, 0.12 \, 0.05 \, \text{b.d.l.} \, 0.15 \, 0.04 \, 0.30 \, 0.21 \, 0.08 \, 0.19 \, 0.10 \, 0.08 \, 0.20 \, 0.03 \, 0.06 \, 0.13 \, Al2O_3 \, 25.08 \, 25.64 \, 26.80 \, 29.56 \, 26.40 \, 21.34 \, 18.56 \, 20.94 \, 19.45 \, 18.89 \, 24.46 \, 20.12 \, 30.76 \, 28.83 \, 32.00 \, \text{MgO} \, 0.22 \, 0.25 \, 0.28 \, 0.28 \, 0.29 \, 0.07 \, 0.15 \, 0.07 \, 0.09 \, 0.17 \, 0.17 \, 0.45 \, 0.37 \, 1.00 \, \text{FeO} \, 0.30 \, 0.47 \, 0.40 \, 0.56 \, 1.17 \, 0.57 \, 1.24 \, 0.90 \, 0.88 \, 1.29 \, 0.76 \, 1.25 \, 0.26 \, 0.35 \, 0.37 \, \text{MnO} \, \text{b.d.l.} \, \text{b.d.l.}$

0.02 -0.01 0.03 0.01 Total 99.03 99.13 99.32 100.47 99.95 99.45 99.99 100.30 101.11 100.69 99.16 99.79 99.59 100.35 99.98 Si 2.64 2.61 2.54 2.39 2.55 2.86 3.00 2.89 2.97 2.98 2.68 2.91 2.31 2.44 2.17 Al 1.34 1.37 1.43 1.58 1.41 1.12 0.96 1.09 1.00 0.97 1.30 1.05 1.66 1.53

 $\begin{array}{c} \text{Ca } 0.35 \ 0.37 \ 0.46 \ 0.60 \ 0.46 \ 0.11 \ 0.01 \ 0.12 \ 0.02 \ 0.03 \ 0.31 \ 0.07 \ 0.70 \ 0.57 \ 0.87 \ \text{Na} \ 0.65 \ 0.62 \ 0.54 \ 0.38 \ 0.54 \ 0.90 \ 0.95 \ 0.86 \ 0.97 \ 0.96 \ 0.66 \ 0.91 \ 0.30 \ 0.41 \\ 0.14 \ \text{K} \ 0.01 \ 0.01 \ 0.01 \ 0.01 \ 0.01 \ 0.00 \ 0.01 \ 0.00 \ 0.01 \ 0.00 \ 0.01 \ 0.00 \ 0.00 \ 0.00 \ 0.00 \ 0.00 \ 0.00 \ 0.00 \ 0.00 \ 0.99 \ 1.00 \ 1.01 \ 1.00 \ 0.99 \ 1.00 \ 1.01 \ 0.97 \ 0.99 \ 1.00 \ 0.99 \ 0.99 \ 0.99 \ 0.99 \ 1.00 \\ 0.99 \ 1.01 \end{array}$

End-Member proportions

 $Ca(Fe,Mg,Mn)Si_3O_8\ 0.82\ 0.76\ 1.45\ 1.82\ 3.20\ 0.14\ 2.37\ 1.85\ 1.40\ 3.02\ 1.50\ 1.92\ 2.16\ 2.35\ 6.41\ KAlSi_3O_8\ 0.59\ 0.38\ 0.23\ 0.41\ 0.03\ 0.07\ 0.01\ 0.78\ 0.36\\ 0.08\ 0.64\ 0.02\ 0.00\ 0.14\ 0.00\ NaAlSi_3O_8\ 6.53\ 61.02\ 53.19\ 37.64\ 52.55\ 87.43\ 94.53\ 85.64\ 95.69\ 94.83\ 65.96\ 89.76\ 29.50\ 41.17\ 12.19\ CaAl_2Si_2O_8\ 33.88\\ 35.74\ 43.69\ 58.03\ 41.88\ 10.27\ 0.00\ 9.58\ 0.61\ 0.25\ 29.69\ 4.86\ 67.22\ 54.70\ 80.16\ (Fe,Mg,Mn)Al_2Si_2O_8\ 0.84\ 1.80\ 1.14\ 1.84\ 2.06\ 1.52\ 1.10\ 1.54\ 1.24\ 1.13\\ 2.01\ 2.64\ 0.95\ 1.23\ 0.89\ []Si_4O_8\ 0.00\ 0.04\ 0.09\ 0.01\ 0.00\ 0.06\ 1.78\ 0.45\ 0.30\ 0.53\ 0.01\ 0.42\ 0.00\ 0.31\ 0.00$

An a 35 37 46 61 46 11 1 12 2 3 32 8 70 58 87

 $Mg\#^{b}$ 54 47 57 47 32 16 17 12 15 20 28 17 76 66 83 a An = Ca / (Ca + Na + K) mole%. b Mg# = Mg / (Mg + Fe) mole%. b.d.l. below detection limit Table 5. Average major and minor elements for glass composition determined with EPMA.

QUE 97008, 12 NWA 8276 NWA 8649, AZ-1-1

c31 c31 c140 c43 c59 c27 c116 (MCEM) (FC-EM)

SiO₂ 67.03 69.60 62.51 66.28 68.90 70.51 65.98 TiO₂ 0.42 0.40 0.52 0.55 0.45 1.06 0.45 Al₂O₃ 16.47 16.12 21.27 17.11 12.25 14.73 17.59 MgO 0.14 0.42 0.63 1.28 0.27 1.07 0.22 MnO 0.45 0.23 0.17 0.24 0.27 0.22 0.13 FeO 4.79 3.70 3.13 4.93 9.89 1.86 4.06 CaO 0.97 0.30 0.30 0.33 0.69 1.85 1.20 Na₂O 8.24 7.92 10.07 8.53 5.28 8.42 9.53 K₂O 1.22 1.36 1.25 1.19 1.15 1.36 1.32 Total 99.74 100.04 99.84 100.45 99.15 101.07 100.49

Table 6. Host oxygen three-isotope ratios of chondrules determined from SIMS analyses.

Chondrule Type n $\clubsuit \clubsuit^{18}$ O Unc. $\clubsuit \clubsuit^{17}$ O Unc. Δ^{17} O Unc. Mg#

OUE 97008, 12 (L3.05)

 $\begin{array}{c} \text{c}12 \text{ I PP } 75.63\ 0.34\ 3.15\ 0.25\ 0.22\ 0.19\ 94\ c31\ II\ PP\ 8\ 4.94\ 0.35\ 3.34\ 0.27\ 0.77\ 0.18\ 82\ c41\ I\ PP\ 8\ 5.21\ 0.34\ 3.34\ 0.22\ 0.63\\ 0.17\ 91\ c68\ I\ PP\ 7\ 5.29\ 0.35\ 3.38\ 0.23\ 0.63\ 0.19\ 96\ c102\ II\ POP\ 8\ 3.51\ 0.52\ 1.64\ 0.35\ -0.18\ 0.14\ 84\ c134\ II\ PP\ 8\ 5.53\ 0.37\\ 3.14\ 0.20\ 0.26\ 0.11\ 84\ c140\ II\ POP\ 8\ 5.15\ 0.37\ 3.47\ 0.25\ 0.80\ 0.11\ 85\\ \end{array}$

NWA 7731 (L3.00)

c33 II POP 6 5.18 0.32 3.25 0.24 0.56 0.18 81 c5 I POP 8 3.82 0.31 3.66 0.20 1.67 0.12 92 c14 II PO 6 5.72 0.35 2.74 0.21 -0.24 0.12 87 c17 II PO 5 4.80 0.31 3.33 0.21 0.84 0.14 82 c24 II PO 8 4.80 0.34 3.37 0.24 0.87 0.13 80 c28 II POP-An 8 5.66 0.34 2.77 0.22 -0.17 0.16 85 c31 I PO 8 -3.56 0.34 -3.86 0.22 -2.01 0.16 100 c34 II PP 5 5.13 0.32 3.24 0.21 0.57 0.15 77 c49 II POP 8 4.30 0.35 3.16 0.22 0.92 0.14 89 c52 II POP 8 4.79 0.34 2.55 0.18 0.06 0.11 76 c73 II PO 8 5.27 0.34 3.56 0.23 0.82 0.15 82

NWA 8276 (L3.00)

MET 00452, 16 (L(LL)3.05)

c85 II POP 6 4.55 0.32 3.13 0.21 0.77 0.16 82

Semarkona (LL3.00)

c55 II PO 7 5.06 0.33 3.11 0.25 0.48 0.20 84

NWA 8649, AZ-1-1 (LL3.05)

c12 II PP 8 4.58 0.34 2.64 0.22 0.25 0.13 85 c27 I PP 6 6.76 0.43 2.57 0.27 -0.94 0.23 94 c62 I PP 5 3.08 0.77 1.53 0.51 -0.07 0.18 98 c116 II PP 8 4.80 0.36 3.04 0.26 0.55 0.17 77

^a Average Mg# of olivine and pyroxene that were analyzed for oxygen isotopes, which are not exactly same as those shown in Tables 1-2

1 Table 7. The Al-Mg isochron regression lines for individual chondrules.

Chondrule Type An a glass n MSWD Slope Unc. $\bullet \bullet$ 26Mg₀ Unc. $(2^6 \text{Al}/2^7 \text{Al})_0$ Unc. Δt_{CAIs} Unc. $(\frac{(\%_0)(\%_0)(\times 10^{-6})(\times 10^{-6})(\text{Ma})(\text{Ma})}{(\times 10^{-6})(\times 10^{-6})(\times 10^{-6})(\times 10^{-6})(\times 10^{-6})}$

 $\begin{array}{c} \text{c}12 \text{ I PP } 19\text{-}43 \ 10 \ 0.96 \ 0.0466 \ 0.0030 \ 0.024 \ 0.050 \ 6.49 \ 0.57 \ 2.13 \ \pm 0.09 \ \text{c}31 \ \text{II PP x } 16 \ 1.1 \ 0.0554 \ 0.0032 \ -0.042 \ 0.054 \ 7.72 \ 0.89 \ 1.95 \\ +0.13/-0.11 \ \text{c}41 \ \text{I PP } 30\text{-}44 \ 9 \ 0.74 \ 0.0493 \ 0.0038 \ 0.035 \ 0.046 \ 6.87 \ 0.67 \ 2.07 \ +0.11/-0.10 \ \text{c}68 \ \text{I PP } 40\text{-}51 \ 9 \ 0.53 \ 0.0507 \ 0.0048 \ 0.013 \ 0.0507 \ 0.066 \\ 0.79 \ 2.04 \ +0.12/-0.11 \ \text{c}102 \ \text{II POP } 55\text{-}66 \ 12 \ 0.92 \ 0.0490 \ 0.0038 \ 0.017 \ 0.048 \ 6.83 \ 0.67 \ 2.07 \ +0.11/-0.10 \ \text{c}134 \ \text{II PP } 43\text{-}48 \ 11 \ 0.87 \ 0.0534 \\ 0.0036 \ -0.004 \ 0.0507 \ 7.44 \ 0.67 \ 1.99 \ +0.10/-0.09 \ \text{c}140 \ \text{II POP } 6\text{-}16 \ \text{x } 12 \ 0.67 \ 0.0515 \ 0.0016 \ 0.046 \ 0.048 \ 7.18 \ 0.75 \ 2.02 \ \pm 0.07 \ NWA \ 7731 \ (L3.00) \\ \text{c}33 \ \text{II POP } 1 \ 11 \ 1.1 \ 0.0491 \ 0.0030 \ -0.010 \ 0.046 \ 6.84 \ 0.80 \ 2.07 \ +0.13/-0.11 \ NWA \ 8276 \ (L3.00) \\ \end{array}$

c22 II POP 8-15 12 1.4 0.0523 0.0015 -0.034 0.042 7.29 0.76 2.01 +0.11/-0.10 c43 II POP 1-6 x 12 0.34 0.0525 0.0020 -0.051 0.048 7.32 0.78 2.00 +0.11/-0.10 c59 II POP x 11 1 0.0551 0.0080 -0.017 0.046 7.68 1.35 1.96 +0.20/-0.17 MET 0.0452, 16 (L(LL)3.05)

c85 II PO 3 9 1.6 0.0517 0.0032 -0.044 -0.044 7.20 0.85 2.02 +0.13/-0.11 Semarkona (LL3.00)

c55 II POP 29-37 10 1.6 0.0498 0.0036 0.012 0.048 6.94 0.65 2.06 +0.1/-0.09 NWA 8649, AZ-1-1 (LL3.05)

 $c12\ II\ PP\ 8\ 8\ 0.73\ 0.0518\ 0.0014\ 0.011\ 0.048\ 7.21\ 0.75\ 2.02\ +0.11/\\ -0.10\ c27\ I\ PP\ 57-73\ x\ 10\ 0.84\ 0.0540\ 0.0054\ -0.015\ 0.050\ 7.52\ 0.88\ 1.98\\ +0.13/\\ -0.11\ c62\ I\ PP\ 87\ 12\ 0.36\ 0.0608\ 0.0056\ -0.027\ 0.050\ 8.47\ 0.78\ 1.86\ +0.1/\\ -0.09\ c116\ II\ PP\ x\ 11\ 1.8\ 0.0680\ 0.0030\ -0.035\ 0.052\ 9.47\ 1.04$

 $1.74 + 0.12 / -0.11 \, ^{a} 2 \, \text{An} = \text{Ca} \, / \, (\text{Ca} + \text{Na} + \text{K}) \, \text{mole} \% \, \text{in plagioclase}.$

Figure 1

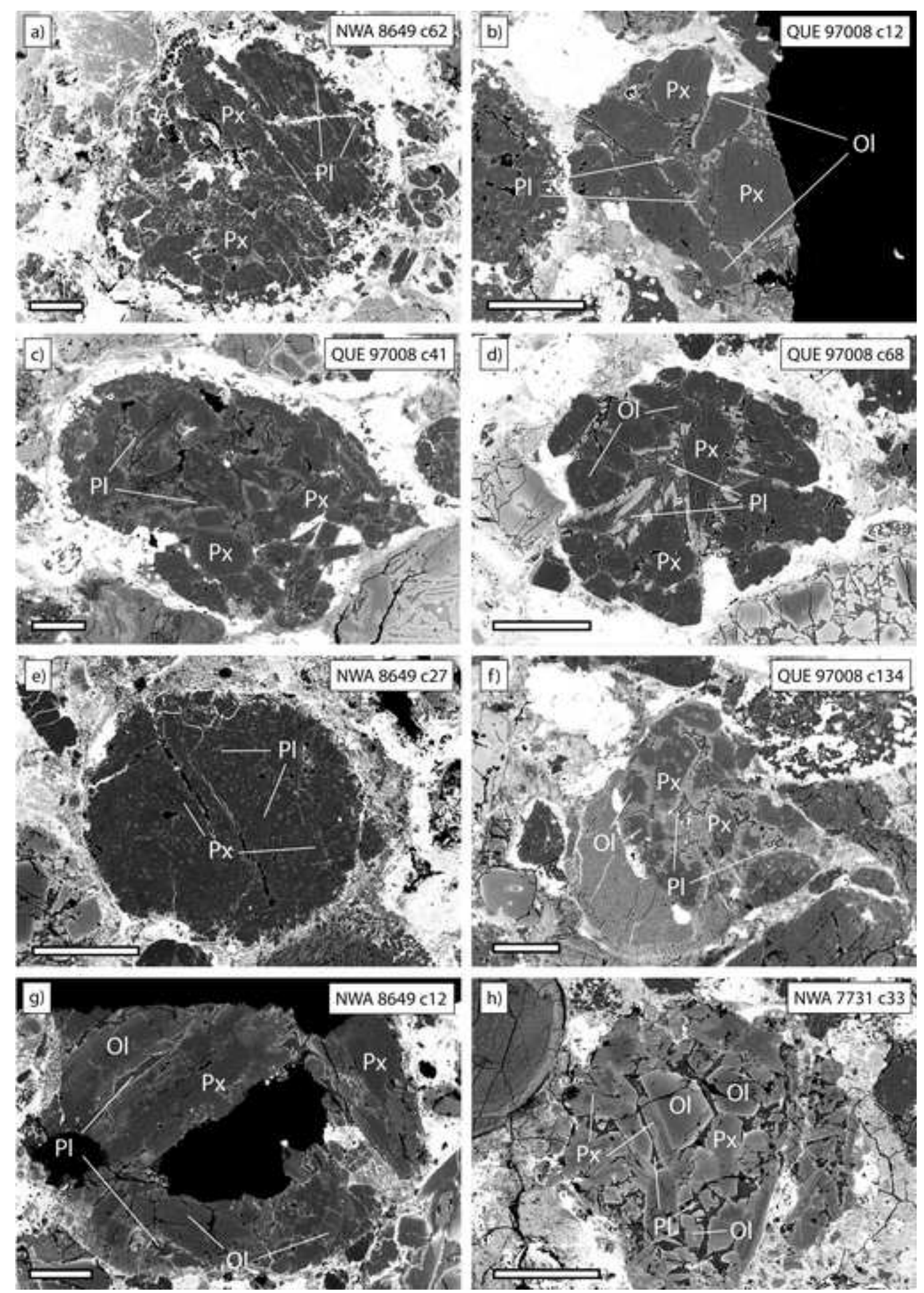


Figure 2

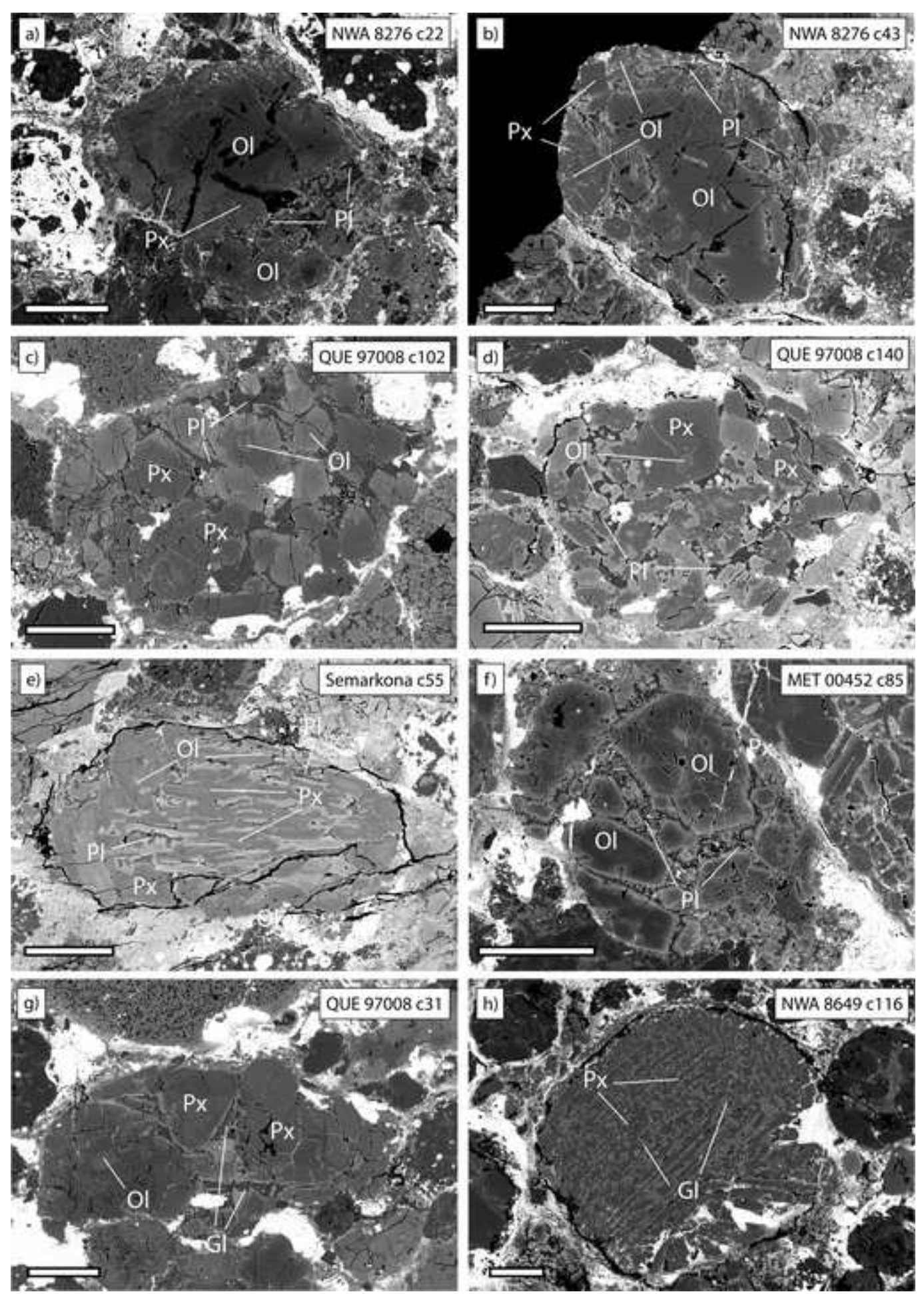
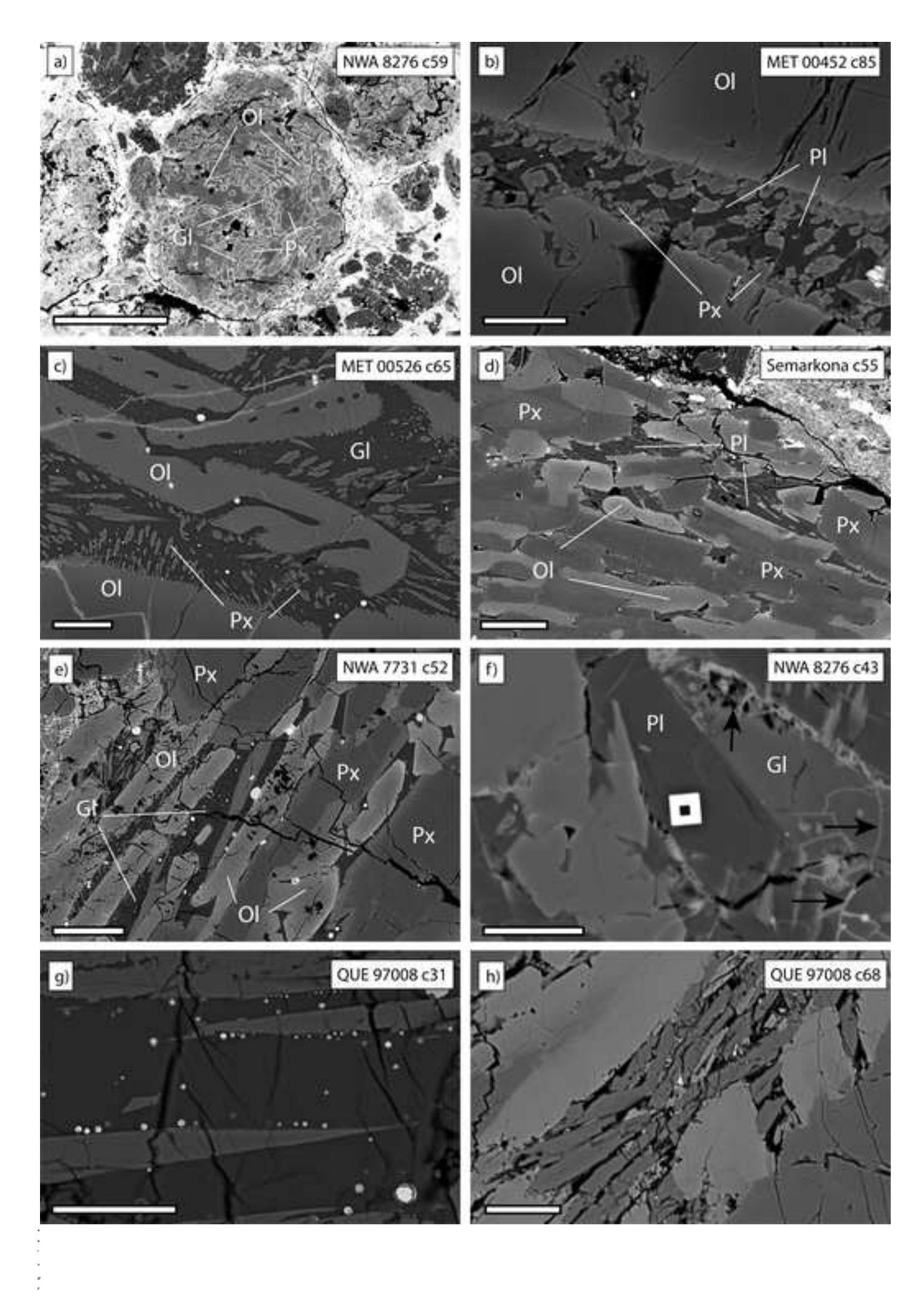


Figure 3



```
Figure 5
```

$$EC^{L}$$
 Figure 6 (LL) (LL) (LL) (L) Mg# = 94, I-PP $^{E}_{C^{L}EC^{L}}Mg# = 77$, II-PP Mg# = 87, II-PO

6 420

(a)

Literature (K10) LL I-PO LL I-POP LL I-PP CH61 (I-PO)

 TF^L

 CCA^M

 PC^{M}

4 32

(b)

Literature (K10) LL type I LL type II

Type II chondrules 4 32

```
(c)
```

```
Literature
An>93 (S21)
LL3 (K10)
```

```
-2
\mathsf{EC}^\mathsf{L}
Type I chondrules
NWA 7731 c31 (PO)
QUE 97008 (L) NWA 8276 (L)
Chondrules for Al-Mg analysis
1
-4 -6
(-12.5, -15.2)
NWA 7731 c5 (POP)
QUE 97008 (PP)
NWA 8649 (PP)
0
NWA 7731 (L)
MET 00452 (L(LL))
NWA 8649 (LL)
Semarkona (LL)
0
An <10 An 10-20 An 20-50
An 50-80 An 80-90 Glass
-4-202468 \delta^{18}O
234567 \delta^{18}O
234567 \delta^{18}O
```